Nickel-cobalt oxide modified with reduced graphene oxide: Performance and degradation for energy storage applications

Alberto Adán-Más, Maria Teresa Silva, Liliane Guerlou-Demourgues, Lydie Bourgeois, Chritine Labrugere-Sarroste, Maria de Fátima Montemor

Nickel-cobalt oxide modified with reduced graphene oxide: performance and degradation for energy storage applications.

Alberto Adán-Más[a,b,*], T. M. Silva[a,c], L. Guerlou-Demourgues[b,d], Lydie Bourgeois[e,f], Christine Labrugere-Sarroste[g], M. F. Montemor[a,*]

[a] Centro de Química Estrutural-CQE, DEQ, Instituto Superior Técnico, Universidade de Lisboa, 1049-001, Lisboa, Portugal

[b] CNRS, University of Bordeaux, Bordeaux INP, ICMCB UPR 9048, 33600 Pessac, France

[c] ADEM, GI-MOSM, ISEL-Instituto Superior de Engenharia de Lisboa, Instituto Politécnico de Lisboa, Lisboa, Portugal

[d]RS2E, Réseau Français sur le Stockage Electrochimique de l'Energie, FR CNRS 3459, France.

[e]Université de Bordeaux, ISM, Groupe de Spectroscopie Moléculaire, F-33405, Talence, France.

[f]Bordeaux INP, ISM, CNRS UMR 5255, F-33405, Talence, France.

[g]PLACAMAT UMS 3626, CNRS-Université de Bordeaux, F-33608 Pessac Cédex, France

[*] Corresponding author. *E-mail addresses*: alberto.mas@tecnico.ulisboa.pt (A. Adán-Más)

Keywords: Electrochemically reduced graphene oxide; Nickel-cobalt oxide; Energy storage; Electrode degradation; Electrochemical impedance spectroscopy

Abstract

Nickel-cobalt oxide is synthesized in combination with electrochemically reduced graphene oxide (Er-GO) by one-step electrodeposition on stainless steel followed by thermal treatment. The presence of reduced graphene oxide leads to enhanced electrochemical response, with a capacity increase from 113 $mA \cdot h \cdot g^{-1}$ to 180 $mA \cdot h \cdot g^{-1}$, and to increased faradaic efficiency and rate capability. Compared to Ni-Co oxide, the addition of reduced graphene oxide increases capacity retention from 58% to 83% after 5000 cycles. The material fade during cycling is studied by means of electrochemical impedance spectroscopy, electron diffraction spectroscopy and scanning electron microscopy. As a result, different degradation mechanisms are identified as source of the capacity decay, such as microstructural cracking, phase transformation and parasitic reactions.

1. Introduction

High-performance, cost-effective and environmentally-friendly electrode materials play a pivotal role in the development of more effective electrochemical energy storage solutions. Electrode materials are classified in different groups according to their electrochemical response, namely: battery-like electrodes, capacitive electrodes and electrodes with an intermediate response (pseudocapacitive, supercapattery, etc.) [1–3].

Many materials are being studied as potential candidates for the next-generation of electrochemical energy storage devices. For instance, for supercapacitor/pseudocapacitor applications, electrodes can be composed of materials as different in nature as carbon-based materials and manganese oxides [4,5]. An alternative is to produce composites consisting of materials that have complementary properties. This is the case of carbon-based materials mixed with polymers and single or mixed transition metal oxides/hydroxides [6–10].

Mixed metal oxides and hydroxides are commonly studied as feasible electrode materials. Examples of that are $Ni_xMn_{1-x}O_y$, $MnCo_2O_4$, Zn_2SnO_4 or $CuFe_2O_4$ amongst many others[11–15]. Of particular interest are nickel-cobalt oxides due to their relative low cost and toxicity, strong redox activity and stable electrochemical response [16]. For instance, one of the most interesting properties of $NiCo_2O_4$ is low proton/cation diffusion resistance and easy electrolyte penetration [17]. Thus, this material is often selected as electrode for charge storage applications.

Several approaches have been used to synthesize nickel-cobalt oxides, such as liquid-phase co-precipitation, sol-gel routes or microwave-assisted synthesis [18–21]. Among all possible techniques, electrodeposition is considered as a flexible and cost-effective route to produce this material. This route enables the tailoring of electrode properties, by adjusting the deposition parameters to create distinct film morphologies, with different composition and porosity, and to achieve optimal electrochemical response. For that reason, electrodeposition

is a promising technique for the scale up of such materials [22]. Besides, since no binders are required, which would decrease the overall electrochemical response, the electron transport to the substrate is facilitated. Moreover, resistances are generally low since most of the active material can be easily exposed to the electrolyte [23]. Nickel-cobalt oxides can be obtained by direct electrodeposition of the parent hydroxide followed by thermal treatment at 300^{o}C for 2 hours [23–25].

To further improve the electrochemical response of nickel-cobalt compounds, its combination with carbon-based materials has been proposed. Several different composites have been studied such as $NiCo_2O_4$ with flexible carbon fabric [26], graphite oxide [27], carbon nanotubes [28] or activated carbon [29]. More recently, graphene and its derivatives have attracted attention for fabricating composites with metal oxides. Due to their attractive properties, *graphenes* have been combined with transition metal oxides and used in different applications, such as drug delivery, catalysis or sensors [30]. Energy storage applications can also greatly benefit from the synergistic combination of the two materials by taking advantage of the large surface area and good conductivity of graphene derivatives. Recent work reports the synthesis of nickel-cobalt oxides and graphene composites by several techniques such as hydrothermal and solvothermal routes [30,31], self-assembly of exfoliated nanosheets with posterior thermal treatment [32], chemical vapour deposition and thermal treatment [33], microwave-assisted synthesis [34] or electrochemical deposition [35]. In some cases, graphene derivatives were used as substrate in the electrodeposition process. For example, Lee et al. prepared a graphene foam by chemical vapour deposition that was covered with double metal oxides by electrodeposition [36]. Shim et al. decorated a nickel foam by electrodepositing GO and then proceeded to the two-step oxide electrodeposition process followed by thermal reduction [37].

In the present work, a composite containing reduced graphene oxide and mixed cobalt-nickel oxide is prepared, by means of a one-step electrodeposition followed by thermal treatment. The results show that presence of reduced graphene oxide (Er-GO)/nickel-cobalt oxide induces relevant changes on the electrochemical activity of the mixed metal oxide. Additionally, the degradation of the composite is studied by means of electrochemical impedance spectroscopy, electron diffraction spectroscopy, cyclic voltammetry and scanning electron microscopy. These measurements reveal important insights to understand the capacity fade that the material suffers in long term use. To the best of the author's knowledge, this is the first time that an in-depth study of the degradation of electrochemically reduced graphene oxide in combination with nickel-cobalt oxide by means of electrochemical impedance spectroscopy together with its physico-chemical characterization after cycling is discussed.

2. Experimental

2.1. Materials

Stainless steel, AISI 304 (Goodfellow) 0.914mm thick, was used as current collector. To ensure homogeneous electrodeposition and absence of contaminants, steel was first polished with emery paper to a rough finish, then cleaned with water and acetone and, finally, air-dried. $Ni(NO_3)_2 \cdot 6H_2O$ and $Co(NO_3)_2 \cdot 6H_2O$ (pro-analysis grade) were obtained from Sigma-Aldrich. A commercial graphene oxide (GO) aqueous solution from Graphenea Tech. Co, with a concentration of $4 g \cdot L^{-1}$ was used. Finally, KOH 1M was used as testing electrolyte. For that purpose, potassium hydroxide purchased from Sigma-Aldrich was used.

2.2. Synthesis of electrodeposited $Ni_xCo_{1-x}O_y$ and $Ni_xCo_{1-x}O_y$/Er-GO composites on Stainless Steel.

The synthesis of the nickel-cobalt oxide and its composite with electrochemically reduced graphene oxide (Er-GO) follows a simple two-step process of electrodeposition followed by thermal treatment. Typically, a 50 mL aqueous solution with a concentration of $2 g \cdot L^{-1}$ of nickel hexahydrated nitrate and $1 g \cdot L^{-1}$ of hexahydrated cobalt nitrate was prepared as electrodeposition electrolyte. For the composite including electrochemically reduced graphene oxide, water was substituted as solvent by a suspension of GO commercial solution diluted to $1 g \cdot L^{-1}$. To ensure good dispersion and layer separation of the aqueous suspension of graphene oxide, it was ultrasonicated for 30 minutes prior to dissolution of the metal nitrates.

Electrodeposition was conducted in a three-electrode electrochemical cell by means of an Interface IFC1000-07087 Potentiostat (Gamry Instruments) in a circular area of 1.6 cm^2. The synthesized materials will be designated throughout the paper as NCOx (from *n*ickel-*c*obalt *ox*ide) and NCOx/Er-GO.

A platinum foil of 2.5x2.5 cm^2 was used as counter electrode and the saturated calomel electrode (SCE) as reference electrode. Pulsed potentiostatic electrodeposition was carried out by means of two cathodic potentials, -0.9V and -1.2V, applied in a 10 second pulse for 40 cycles. After electrodeposition, the electrodes were washed with distilled water and dried at room temperature for 24-48h. Finally, thermal treatment was performed by heating the composite materials at 300^oC for 3 hours in normal atmosphere, as it is reported in literature that it is sufficient for the complete transformation of hydroxides to oxides and shows and optimal electrochemical response[38,39].

Electrodeposition has been performed on top of stainless steel for several reasons. First, it is an inexpensive, non-toxic and completely recyclable substrate with excellent conductive properties. In addition, the degradation mechanism of the active material is studied by means of EIS. Stainless steel is selected to confine the EIS signal to the active material since it does not increase porosity, has no contribution to the final electrochemical response, does not introduce relevant resistance and it is corrosion resistant.

It is worth mentioning that the mass of the samples always varied between 0.15 and 0.2 mg, which was determined by means of a micro-balance Sartorius MC5-0CE with an accuracy of 0.01mg.

2.3. Electrochemical Study of $Ni_xCo_{1-x}O_y$ and $Ni_xCo_{1-x}O_y$/Er-GO composites.

All tests were performed in a three-electrode electrochemical cell with KOH 1M as electrolyte using the same electrochemical equipment as for electrodeposition. Cyclic voltammetry, galvanostatic charge-discharge (GCD), electrochemical impedance spectroscopy (EIS) and capacity retention with GCD cycling were used to study the electrochemical response of the materials. Cyclic voltammetry was performed in the potential range from -0.2V to 0.7V vs. SCE at different scan rates (10-500) $mV \cdot s^{-1}$. GCD was carried out at different current values from 1 to 10 $A \cdot g^{-1}$ in the 0.0V to 0.45V potential range. EIS was carried out at two different potentials,

corresponding to two different charge states of the material, this is, discharged at -0.2V and charged at 0.45V. First, a conditioning pre-step was done by applying a voltage of interest for 1000 s. Then, EIS was measured by applying a sinusoidal perturbation with 10 mV of amplitude (rms) in the frequency range 0.01 – 10^4 Hz. Finally, capacity retention testing was performed for the nickel-cobalt oxide material by charging and discharging the material 5000 times at a current density of 8 $A \cdot g^{-1}$.

2.4. Characterization

Surface morphology and chemical composition of the different materials were studied by means of scanning electron microscopy (SEM) direct imaging, energy dispersive X-ray spectroscopy (EDS), transmission electron microscopy (TEM), X-ray photoelectron spectroscopy (XPS) and Raman spectroscopy.

SEM imaging was obtained by means of an FEG-SEM JEOL JSM 7800F Prime coupled with an EDS detector (EDS SDD X-Max 80mm^2 Oxford Instruments AZtecEnergy detector, which is located at the centre of micro-characterization Raimond Castaing, Toulouse). Two detectors were used in the measurement, compositional and upper electron detector.

TEM images and EDS were obtained with a TEM JEOL 2200FS coupled with an EDX JEOL Si-Li working at 200k located at the Platform of Materials Characterization of Aquitaine (PLACAMAT). The image resolution is 0.19 nm and the EDS point resolution is 1.5 nm. Since the materials were attached to the conductive substrate, a portion of the thin layer had to be scratched and dispersed in ethanol on top of a carbon-coated gold grid.

Raman spectra were recorded using a Jobin Yvon Horiba Labram HR-800 micro-spectrometer with a 514.5 nm excitation wavelength (Ar^+ laser) and a power adjusted to ca. 50 µW to avoid any degradation of the sample.

XPS surface analysis was obtained using a ThermoFisher Scientific K-ALPHA spectrometer with a monochromatized Al Kα source (hv = 1486.6 eV) and a 200 microns spot size. Before insertion of samples in the analysis chamber, a pressure of $3 \cdot 10^{-7}$ mbar was always reached in the load lock chamber. High-resolution photoionization spectra were acquired for the elements (C1s, Ca2p, Cl2p, Co2p, Co3p, Cr2p, Fe2p, Fe3p, N1s, Ni2p, Ni3p, O1s, and Si2p) by using a constant pass energy of 40 eV although wider spectra in the 0 to 100 eV range were first obtained at the constant pass energy of 200 eV. Charge neutralization was applied during analysis. High resolution spectra were fitted and quantified using the AVANTAGE® software provided by ThermoFisher Scientific.

Furthermore, XPS was also used to characterize the material and to identify its surface chemical state and to discriminate the oxidation state of nickel and cobalt. For that reason, the main elements considered were nickel, cobalt and oxygen. The spectra were corrected to obtain a C1s spectral component binding energy of 284.7 eV. Moreover, a standard Shirley background was generally used except for those cases in which relevant information was lost, in which linear background subtraction was considered.

Grazing incident X-ray diffraction (GIXD) analysis were performed, however, no meaningful signal could be obtained due to the thinness of the deposited layer and its nanostructured nature.

3. Results and Discussion

3.1. Physico-Chemical Characterization

3.1.1 Morphological Characterization

Fig. 1. shows the morphology of $Ni_xCo_{1-x}O_y$ (NCOx) and $Ni_xCo_{1-x}O_y$/Er-GO (NCOx/Er-GO) obtained by electrodeposition and thermal treatment. Scanning electron microscopy results are shown in two different detector modes: upper electron detector, whose signal is obtained at very close distance from the sample, to enhance morphological details, and compositional (COMPO) mode, that collects secondary electrons and displays a different signal, which depends on the atomic mass of the elements present in the sample. NCOx shows a relatively porous morphology that seems composed of small areas of aggregated nanosheets with sizes around 200-500 nm. This is similar to the flake-like structure presented in previous work, but with a greater level of agglomeration [40,41]. SEM images of the parent hydroxides have been included for comparison purposes (Fig. S1). Some spike-like features are still observable although they do not present relvant compositional differences. Moreover, this aggregated nanosheet-like structure with no apparent order forms densely-packed percolation networks whose pores can be differentiated as darker areas at the compositional image (Fig. 1.a-2) in accordance with literature [9,10]. This suggests that, in this case, the nanosheet-like structure is aggregated to better accommodate strain, becoming more densely packed, while conserving some of the features at a superficial level.

The morphology of the Er-GO containing composite is, as observed by SEM in Fig. 1.a-3,4, is distinct of that of the material without carbon. In this case, the said aggregation has not occurred, and the material presents the nanosheet-based structure on the top of the

carbonaceous material. Er-GO displays micrometric wrinkles and defects and seems to cover all the substrate. Then, on top of the carbon-based material, Ni-Co oxides could be found. This structure is similar to other reported Ni-Co oxides [42]. NCOx/Er-GO presents morphology similar to the non-thermally-treated precursor which suggests that, by dispersing the nickel and cobalt nanoflakes on top of the reduced graphene oxide wrinkles, aggregation of said flakes is avoided. In conclusion, when no electrochemically reduced graphene oxide is present, the material presents higher strain that accommodates under thermal treatment thanks to the formation of aggregates. Once Er-GO is introduced, the material morphology remains unchanged during thermal treatment [35].

Pristine graphene has very high conductivity (>3000 $W \cdot mK^{-1}$) [43,44]. Although the properties of graphene oxide and reduced graphene oxide are not comparable to that of pristine graphene, it has been reported that reduction of graphene oxide and thermal treatment enhance the thermal conductivity of the material; in fact, it increased up to 10^6 times as reduction at low temperature (<240^{o}C) progressed [45] and it enhanced the longer the thermal treatment [46]. It is possible that the inclusion of a better thermal conductor inhibits the structural variation of the material by a homogeneous distribution of temperature in the material. Thus, thermal treatment does not have preferential areas while, in the case of NCOx, which in principle has poorer thermal conduction, the material aggregates as the thermal distribution is inhomogeneous. However, this phenomenon is yet poorly understood and requires further understanding to fully corroborate this statement.

The transmission electron microscopy (TEM) images are shown in Fig. 1b and it can be observed that NCOx consists of randomly oriented grains. These grains have very small coherent domains of approximately 2 to 5 nm. This morphology is also in accordance to previously reported literature [31,47]. Therefore, aggregates of 200-500 nm observed by SEM consist of grains with very small coherent domains of 2-5 nm diameter.

For the graphene-based material, the wrinkles of the carbon flakes are observed at higher magnification. Nonetheless, if a closer view to the surface morphology is taken, small features with very small coherent domains are present (see Fig. S2). An image of the FFT obtained for the high-resolution image of the composite material is also included in the supplementary material, which evidences the polycrystalline nature of the synthesized oxide. Thus, it can be deduced that the oxide material is deposited on top of the carbon flakes, in accordance with the SEM results. These small features correspond to the spike-like structures observed by SEM that can be better resolved by HRTEM.

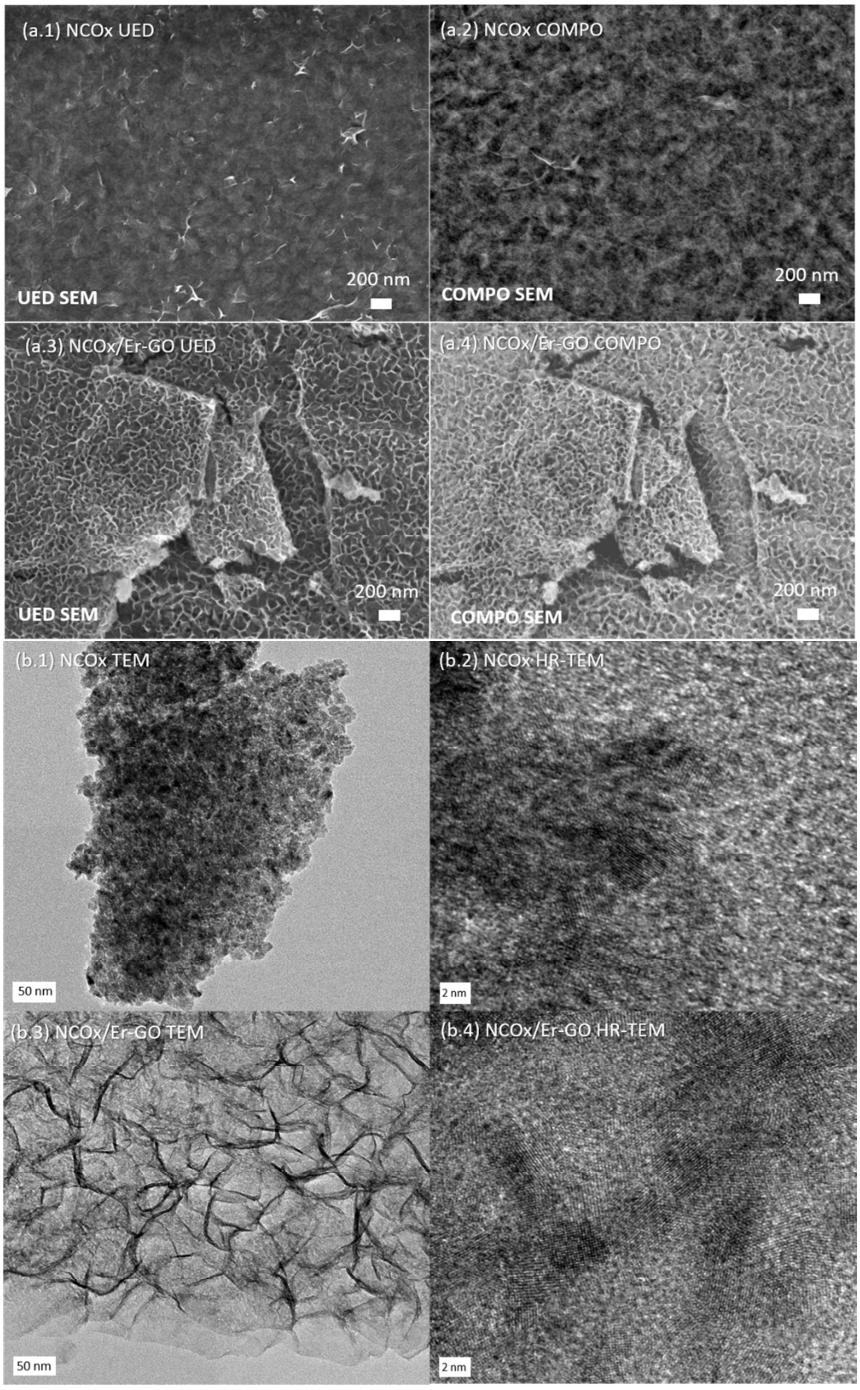

Fig. 1. SEM images of **(a.1)** NCOx obtained with an upper-electrons detector (UED), **(a.2)** and a compositional detector (COMPO). **(a.3)** NCOx/Er-GO obtained with an UED and **(a.4)** a COMPO detector and TEM images of **(b.1,2)** NCOx and **(b.3,4)** NCOx/Er-GO.

3.1.2 Chemical Characterization

EDS results, presented in Fig. S3, show the homogeneous distribution of nickel and cobalt atoms evidencing the good distribution of both metals that integrate the oxide material. Moreover, the good coverage of the carbon flakes by nickel-cobalt oxide can also be observed for the Er-GO containing composite. If the EDS atomic percentage ratio between nickel and cobalt is considered for the semi-quantitative evaluation for the material composition, a nearly 2:1 Nickel-Cobalt ratio is found, resulting in an empiric formula of $Ni_{0.63}Co_{0.37}O$ for both the material with and without Er-GO; which is in accordance to the molar ratio used in the electrolyte for electrodeposition. Similar semi-quantitative results were obtained by means of XPS, in which the empiric formula considering the Ni/Co ratio obtained is $Ni_{0.64}Co_{0.36}O$ for NCOx and $Ni_{0.68}Co_{0.32}O$ for NCOx/Er-GO. Thus, this material can be understood as a mixed nickel-cobalt oxide. XPS was done to further elucidate the composition of the material. For that purpose, the photoionizations of Nickel 2p3, Cobalt 2p3, Oxygen 1s and Carbon 1s were investigated. It shall be noted that carbon signal is present in both EDS and XPS results of NCOx due to adventitious carbon contamination, present in samples exposed to air [48,49], and residual carbonates from the interslab space of α-Ni-Co$(OH)_2$ [50,51]. Neither Iron nor Chromium were detected, which evidenced complete coverage of the substrate during the electrodeposition. XPS results are shown in Fig. 2.

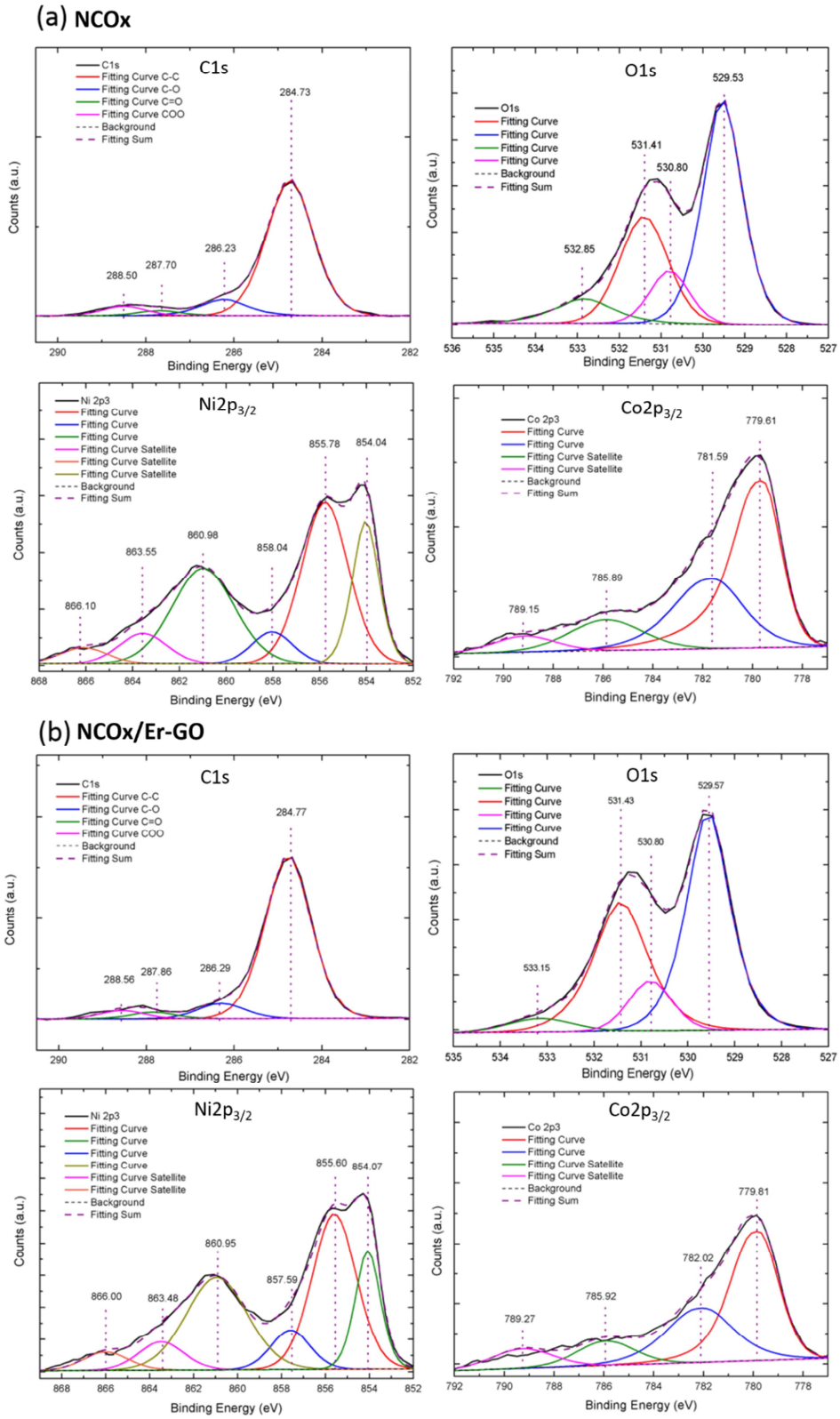

Fig. 2. X-ray photoelectron spectroscopy results for the elements Carbon 1s, Oxygen 1s, Nickel 2p3/2 and Cobalt 2p3/2 for the composites (**a**) NCOx and (**b**) NCOx/Er-GO.

The assignment of discrete binding energy values is used to identify different oxidation states for nickel metal and nickel hydroxides, oxides and oxyhydroxides. However, due to the splitting nature into multiplet contributions and the overlaps of the main line and satellite peaks in the most intense Ni 2p spectra, this approach has been substituted by multi-component spectral envelopes. These are done with the minimum possible number of components and their correspondent shake-up and plasmon satellites [52–54].

The main contribution to the primary peak is based on Ni^{2+} and Ni^{3+} chemical states, although their contributions cannot be perfectly resolved, even when there is a main peak as reference. Nonetheless it is observed that Ni^{3+} tends to appear at higher binding energies [54]. Also, a third contribution in the region between the main line multiplet and the related satellites is considered in the fitting and represents the combined losses at 4.3 eV, 6.0 eV and 7.4 eV due to intra- and inter-band transitions allowed by breakdown of dipole selection rules with delocalized electrons in polycrystalline samples, as described by Hagelin-Weaver et al. [53,55]. In conclusion, the experimental signal has been reconstructed by fitting to six Voigt peaks that have been assigned to different electronic configurations after the creation of the 2p core-hole upon photoemission [56]. Three main peaks are used in the fitting of the main multiplet for nickel and are assigned to a cluster mode with a final configuration of cd^9L for the peak at lowest BE, d^8:cd^9L configuration from surface-sensitive components for the peak at around 855.6 eV and a cd^9:d^7 for the third component of the multiplet. Besides, three satellite/plasmon peaks are considered to contribute to the final signal. They arise from energy losses corresponding to surface plasmons and bulk plasmons, corresponding to $cd^{10}L^2$ and cd^8 cluster model final state configurations, and weaker shake-up contributions for the component at higher BE. These different configurations come from the overlap of the frozen ground state and the unscreened final state and the effect of neighbouring electrons, and associate charge transfer processes between the ligand anions and the Ni cation, coming from adjacent Ni-O clusters. Both the area and the position are considered in the fitting of nickel [54,56].

In this case, there is a major contribution from Ni (II)/Ni(III) centred at 854.0/855.7 eV and a third component corresponding to combined losses. It can be observed that the main peak becomes partially resolved, showing two decreasing maxima. This is only observed in nickel-oxide configurations. Also, three other peaks, corresponding to shake-up satellites and plasmons at 6, 9 and 12 eV higher binding energies than the main peak, are present. Given these peak positions, and the contribution of each component to the total signal (as seen in supplementary information table S1, related to XPS identification work performed by Biesinger et al. [53] and the calculations presented by Gupta and Sen [55,57]) nickel can be identified, in this case ,to be coordinated with oxygen atoms in its nickel oxide form.

Cobalt 2p3 was fitted with an asymmetric main peak and two plasmon loss peaks 3eV and 5eV above the main peak, which constitute the surface and bulk plasmons, respectively [52]. The main peak, similarly to the case for nickel, is resolved in two main components, associated to different chemical species despite the significant overlap in binding energy that they have. In the de-convolution of the peak there is an intense main peak centred at approximately 779.7 eV. Given the low value for this binding energy, cobalt may be present in its oxide form instead of the oxyhydroxide or hydroxide alternatives [58]. The presence of a broad peak centred at around 781.8 eV evidences the divalent nature of the oxide. Two satellite peaks are present in the case of cobalt related configuration and are associated to either coupling between unpaired electrons (multiplet splitting) or multiple electron excitation (shake-ups). Although the peak centred at 789.2eV would be present in all the possible configurations, Co(II) oxides are distinguished from Co(III) oxides by the absence of multi-electron excitation satellites in the latter. Given the fact that a peak is centred at 785.9 eV and that lower binding energies to what would be expected for cobalt hydroxide and its contribution to the overall signal, cobalt can be unequivocally identified to be in the oxide form [58].

In addition, four peaks are required to fit the oxygen 1s envelope. The main intense peak is centred at 529.6 eV. This peak is characteristic for both nickel and cobalt oxide and does not have a relevant contribution in isolated nickel/cobalt hydroxide [58]. Three peaks, of lower intensity, centred at 530.8 eV, 531.4 eV and 532.9 eV are also included. The first peak at lower binding energies is associated to oxygen from hydroxyl ions. The higher binding energy peaks are ascribed to hydroxyl, carbonate ions and other oxygen ions and possible surface contamination. If the contribution to the total signal is analysed and compared to literature, as presented in table S1, results also agree with Ni-O and Co-O bonding nature. For that reason, it can be concluded that the phase present is a mixed oxide with formula $Ni_xCo_{1-x}O_y$.

Fig. 3 shows the Raman spectra obtained for the composites. Raman spectroscopy is a powerful technique extensively used in the characterization of graphene derivatives, enabling the evaluation of defects and disorders associated to its structure. As expected for NCOx/Er-GO, two main peaks are present at approximately 1368 cm^{-1} and 1594 cm^{-1}, corresponding to the D and G bands, respectively. The former is associated to local defects and disorders and is originated k point phonon breathing with A_{1g} symmetry; the latter is related to sp^2 carbon atoms E_{2g} vibrational mode [41,59]. Note that the shoulder detected around 1550 cm^{-1} is observed for some other carbon nanostructures [63,64]. The signature obtained for NCOx/Er-GO after thermal treatment is different from graphene oxide and as-synthesised reduced graphene oxide (Fig. S4) and indicates a successful reduction of the graphene derivative and an effect of thermal treatment on signal intensity on the D and G bands.

Usually, the ratio between the integrated intensity of the D peak and the G peak offers information regarding the average size of the sp^2 domains and the charge transfer between carbon and other compounds [60]. Then, a higher the I_D/I_G ratio is correlated to smaller sp^2 domains. In our case, this ratio has a value of 0.62, which indicates large sp^2 domains [61]. It has been currently observed in literature that the signal of the D peak is reduced after

temperature treatment, indicating either an improved quality of the graphene film [62,63] or an agglomeration of the carbon-based material that induces a recovery of its graphitic nature. This change in the I_D and I_G intensities is shown in Fig. S4. Thus, during electrodeposition, electrochemically reduced graphene oxide is produced [35] and after thermal treatment graphene layers are likely to improve their quality by the restoration of the Csp^2 matrix [64]. Although an interaction between the different carbon layers is also possible, due to their complete coverage with nickel-cobalt oxide, as observed by EDS results presented in Fig. S3, re-stacking is unlikely and a restoration of the Csp^2 is considered.

In addition, there are three signals at ca. 480, 550 and 655 cm^{-1}, associated to nickel-cobalt oxide. These bands correspond to Ni-O and Co-O vibrations and can be assigned, by analogy, to the E_g, F_{2g} and A_{1g} Raman-active modes of the ideal cubic spinel $NiCo_2O_4$ [65,66]. It is worth mentioning that there is a small band shift for NCOx/Er-GO that is related to the direct charge transfer between rGO and (Ni-Co)O [60]. Only Co-O and Ni-O vibrational modes are observed, this is, no -OH signal is detected between 3000 and 4000 cm^{-1}, indicating successful de-hydroxylation of the materials. This is in accordance with previously reported literature [65,66]. Thus, Raman spectra confirm the presence of a cobalt-substituted nickel oxide phase on top of thermally treated highly reduced graphene oxide with a restored 2D lattice.

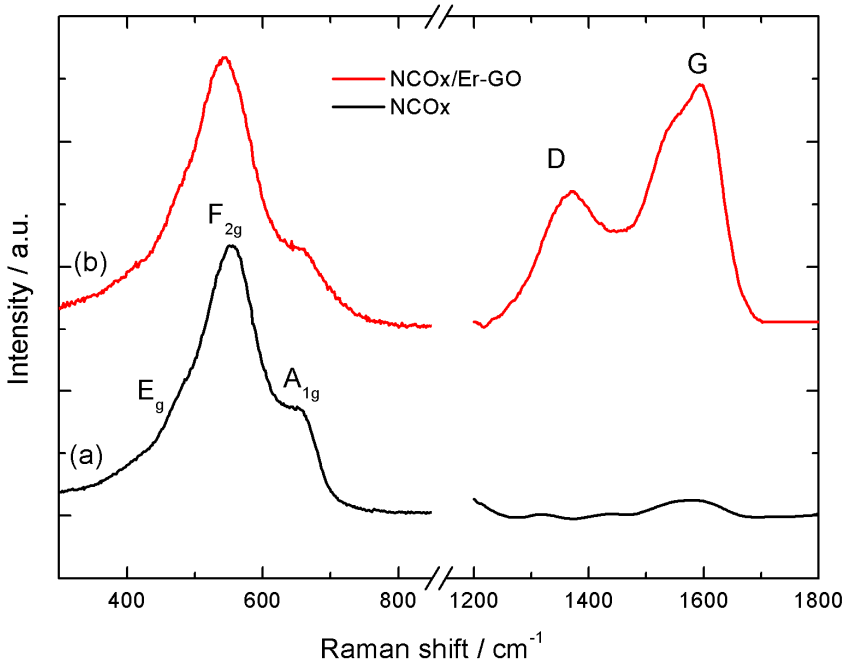

Fig. 3. Raman spectra for (**a**) NCOx and (**b**) NCOx/Er-GO.

3.2. Electrochemical Characterization

Results for cyclic voltammetry, obtained at 50 $mV \cdot s^{-1}$ in the -0.2 V to 0.5 V (vs. SCE) potential range, and galvanostatic charge-discharge, obtained at 1 $A \cdot g^{-1}$ in the 0.0 V to 0.45 V (vs. SCE) range, for NCOx and NCOx/Er-GO obtained in KOH 1M are presented in Fig. 4a.

As expected for a nickel-cobalt oxide-based material, the voltammogram presents a peak in the anodic wave, centred at 0.33 V and 0.30 V for the material without and with reduced graphene oxide respectively, and a counter-peak in the cathodic wave centred at 0.23V and 0.20 V for NCOx and NCOx /Er-GO, respectively.

The reported charge-discharge reaction for nickel oxide is [67]:

$$NiO + OH^- \leftrightarrow NiO(OH) + H_2O + e^- \text{ (eq. 1)}$$

Given that reaction, the charge-discharge reaction for the present material can be considered to be as exemplified in eq. 2:

$$Ni_{1-x}Co_xO_y + 2OH^- \leftrightarrow Ni_{1-x}Co_xO(OH) + H_2O + e^- \text{ (eq. 2)}$$

It is also worth noting that these reactions do not show the exact stoichiometry and are only intended to exemplify the oxidation state variation of nickel and cobalt during the charge-discharge process.

As far as the maximum current peak ratio ($I_{max,\ anodic}/I_{max,\ cathodic}$) is concerned, if the ratio of the intensity of the cathodic peak against the intensity of the anodic peak is calculated, it is approximately 1.4 in both cases, indicating a similar and partial irreversibility of the reaction. Again, this difference may result in the lowering of capacity efficiency with continuous charge-discharge.

Nonetheless, the most relevant feature is the increase in the total area of the voltammogram when Er-GO is introduced. This is consequence of an increase in capacity due to the synergistic response of Ni-Co oxides and Er-GO [34,35].

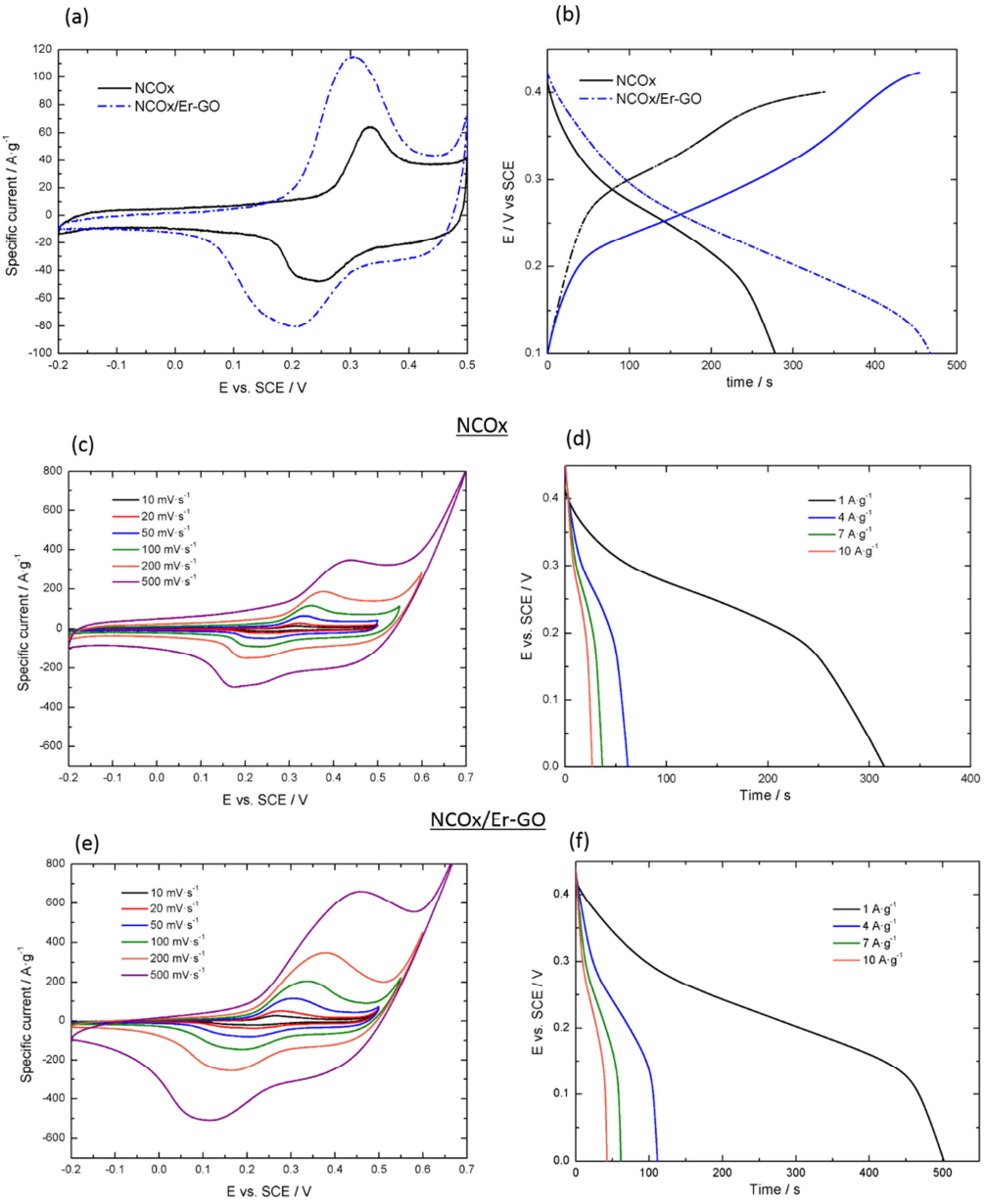

Fig. 4. Cyclic Voltammetry and Galvanostatic charge-discharge results comparison at 50 $mV \cdot s^{-1}$ and 1$A \cdot g^{-1}$ respectively for (**a**) NCOx and (**b**) NCOx/Er-GO. Cyclic Voltammetry for (**c**) NCOx and (**e**) NCOx/Er-GO at scan rates from 10-500 $mV \cdot s^{-1}$ and Galvanostatic Charge-Discharge Curves at current densities from 1-10 $A \cdot g^{-1}$ for (**d**) NCOx and (**f**) NCOx/Er-GO measured in KOH 1M.

The cyclic voltammetry response with the scan rate is presented in Fig. 4c,e, in the scan rate range from 10 $mV \cdot s^{-1}$ to 500 $mV \cdot s^{-1}$, and the results show that both materials present very good scan rate capabilities. The two characteristic peaks are always present and the form of both

the cathodic and the anodic wave is kept for a wide range of scan rates. Very high scan rates can be achieved for the nickel-cobalt oxide material by means of electrodeposition. This has been observed in other films for energy storage applications obtained by means of electrophoresis or electrodeposition [35,68], however, this is rarely seen in nickel-cobalt metal oxides where the highest reported scan rates are usually 100 $mV \cdot s^{-1}$ or lower [24,25,69,70]. This may be the result of a combination between good substrate-electrode contact and enhanced electrode-electrolyte interaction as a consequence of morphology tailoring and absence of binders.

Finally, when the scan rate is increased, a shift of the anodic peak towards more positive potentials is observed, while the cathodic counterpart is displaced towards more negative potentials. Furthermore, the current density increases with faster scan rates. This is a consequence of the polarization effects, evidencing the quasi-reversible nature of the redox processes in the system and smaller diffusion layers associated to faster redox reactions with increased scan rate [71,72].

In conclusion, the graphene derivative does not alter the electrochemical signal of the material but does enhance the electrochemical response, resulting in an augmentation of the capacity due to the synergistic effect between Ni-Co oxide and reduced graphene oxide. This is also observable in the galvanostatic charge-discharge curve (Fig. 4b).

On the one hand, the capacity values obtained from the discharge curves in KOH 1M (curves presented in Figure 4.d,f and values shown in table 1) go from 113.4 $mA \cdot h \cdot g^{-1}$ at $1A \cdot g^{-1}$ to 95.5 $mA \cdot h \cdot g^{-1}$ at an applied specific current of 10 $A \cdot g^{-1}$ for NCOx. On the other hand, the values obtained for NCOx/Er-GO range from 180.6 $mA \cdot h \cdot g^{-1}$ to 152.6 $mA \cdot h \cdot g^{-1}$ at 1 and 10 $A \cdot g^{-1}$ respectively. Indeed, an increased capacity of approximately 159% at $1A \cdot g^{-1}$ is obtained, together with a better capacity rate when thermally treated electrochemically reduced graphene oxide in introduced.

Several groups have studied the electrochemical performance of Ni and Co oxides before, although sometimes wrongly reported as capacitance despite their redox reaction based on a phase transformation and a voltage-dependent response in their galvanostatic charge-discharge curves as explained by Brousse et al. [73]. Li et al. have reported 1523.0 $F \cdot g^{-1}$ at 2 $A \cdot g^{-1}$ in the 0.05V to 0.55V potential range (vs. Hg/HgO) in KOH 2M, excellent rate capability and cycling stability (94% retention after 1000 cycles) for electrodeposited $Ni_{0.61}Co_{0.39}$ oxide [25] while Gong et al. reported 1479 $F \cdot g^{-1}$ at 1$A \cdot g^{-1}$ in the 0.0V to 0.5V potential range and a capacity retention of a 82% after 3000 cycles in the same electrolyte [74].

Various nickel-cobalt oxide/carbon composite materials have also been prepared, for instance, Wang et al. prepared Ni-Co oxide nanocages on top of graphene nanoribbons by chemical precipitation followed by hydrothermal reaction resulting in 937.8 $F \cdot g^{-1}$ at 1$A \cdot g^{-1}$ in the 0.00V to 0.45V potential range (vs. RHE) and 97% capacity retention after 1000 cycles in 2M KOH [75]. Indeed, nickel cobaltite has been combined with reduced graphene oxide by different routes. It has been obtained by microwave-assisted synthesis [34], surface modification of nickel-cobalt hydroxides and self-assembly of positively charged nanosheets [32,76] and hydrothermal synthesis [16]. When prepared by hydrothermal method, without surfactants, $NiCo_2O_4$@rGO displays 737 $F \cdot g^{-1}$ at 1$A \cdot g^{-1}$ in KOH 2M in a 0.7V potential window and 94% retention after 3000 charge-discharge cycles. Similar results were obtained for the microwave-assisted synthesis. Interestingly, a capacity of 735 $F \cdot g^{-1}$ (83% retention) for an applied current as high as 33 $A \cdot g^{-1}$ was reported. The electrodeposition of nickel-cobalt oxide on top of CVD graphene@Ni foam was reported by Shim et al. [77], displaying 2356 $F \cdot g^{-1}$ at 2$A \cdot g^{-1}$ in the -0.1V to 0.35V vs. SCE potential range and a capacity retention of a >100% capacity retention after 1500 cycles. They also reported the electrodeposition of graphene on top of Ni foam, with a subsequent electrodeposition of Ni-Co hydroxide and thermal treatment. In this case, a value of 2260 $F \cdot g^{-1}$ in the -0.1V to 0.3V potential range at 1$A \cdot g^{-1}$ and a retention of a 92.8% of the

initial capacity were obtained [37]. Results in the present work are, therefore, comparable to the previous reported literature considering the electrochemical inactivity of stainless steel.

Table 1

Values of capacity calculated at current densities ranging from 1 to 10 $A \cdot g^{-1}$ for NCOx and NCOx/Er-GO.

Current Density ($A \cdot g^{-1}$)	C_{NCOx} ($mA \cdot h \cdot g^{-1}$)	$C_{NCOx/Er\text{-}GO}$ ($mA \cdot h \cdot g^{-1}$)
1	113.4	180.6
4	88.9	160.2
7	92.5	154.8
10	95.5	152.6

Both materials display excellent rate capability, with a minimum capacity retention of 78% in the case of NCOx and of 84% in the case of NCOx/Er-GO when 10 $A \cdot g^{-1}$ are applied. Again, it is worth noticing the overall better rate capability of the material in the presence of electrochemically reduced graphene oxide, in accordance with literature [32,78]. This may be the result of better electron transport induced by the Er-GO matrix, in which the nickel-cobalt oxide is sustained as observed by SEM and TEM.

Faradaic efficiency is also an important characteristic that shall be studied. If the charge versus discharge time for the composite materials is evaluated ($t_{discharge}/t_{charge}$) at 1 $A \cdot g^{-1}$, a ratio of 0.88 is obtained for NCOx while a value of 1.01 is obtained for NCOx/Er-GO. This shows better faradaic efficiency when Er-GO is integrated. While the pure nickel-cobalt oxide material shows relevant faradaic losses in the charge-discharge process, it is optimized for NCOx /Er-GO. This may be the result of a better electron transfer since Er-GO may create a matrix that acts as a secondary substrate and enhances the conduction of electrons and, therefore, better reversibility of the reaction [79].

Finally, another relevant feature that can be observed in the charge-discharge curves is the progressively descending plateau. If the discharge curve of NCOx is considered, a nearly linear descending plateau begins at 0.30V that ends at approximately 0.2 V whereas, in the case of NCOx/Er-GO, the plateau is prolonged from 0.29 V to 0.14 V. Thus, the response, which is voltage dependent, extends its effective potential range in the presence of Er-GO.

3.3. Cycling Degradation Mechanism

One of the main goals when synthesizing a new material for energy storage applications is to obtain increased durability in their charge-discharge cycling. In fact, end-of-life criteria for both supercapacitors and batteries is generally considered when their capacity/capacitance is reduced in a 20-30% or there is an increase of a 100% in the equivalent series resistance [80,81].

To evaluate the sources of capacity and degradation phenomenon in NCOx and NCOx/Er-GO, different techniques were applied. First, a durability test during 5000 cycles of charge-discharge at 8 $A \cdot g^{-1}$ (Fig. 5a). EIS and cyclic voltammetry were performed after 0, 150, 750, 1500 and 5000 cycles together with the physico-chemical evaluation by means of SEM/EDS before and after cycling.

NCOx has a capacity retention of 58% after 5000 cycles, while a 70% and 80% end-of-life criterion occurs after 1059 and 563 cycles respectively. On the other hand, NCOx/Er-GO maintains a capacity retention of 83.2% even after 5000 cycles, showing much better cycle durability and increased performance compared to its analogous material without electrochemically reduced graphene oxide. Also, an initial increase in capacity is observed.

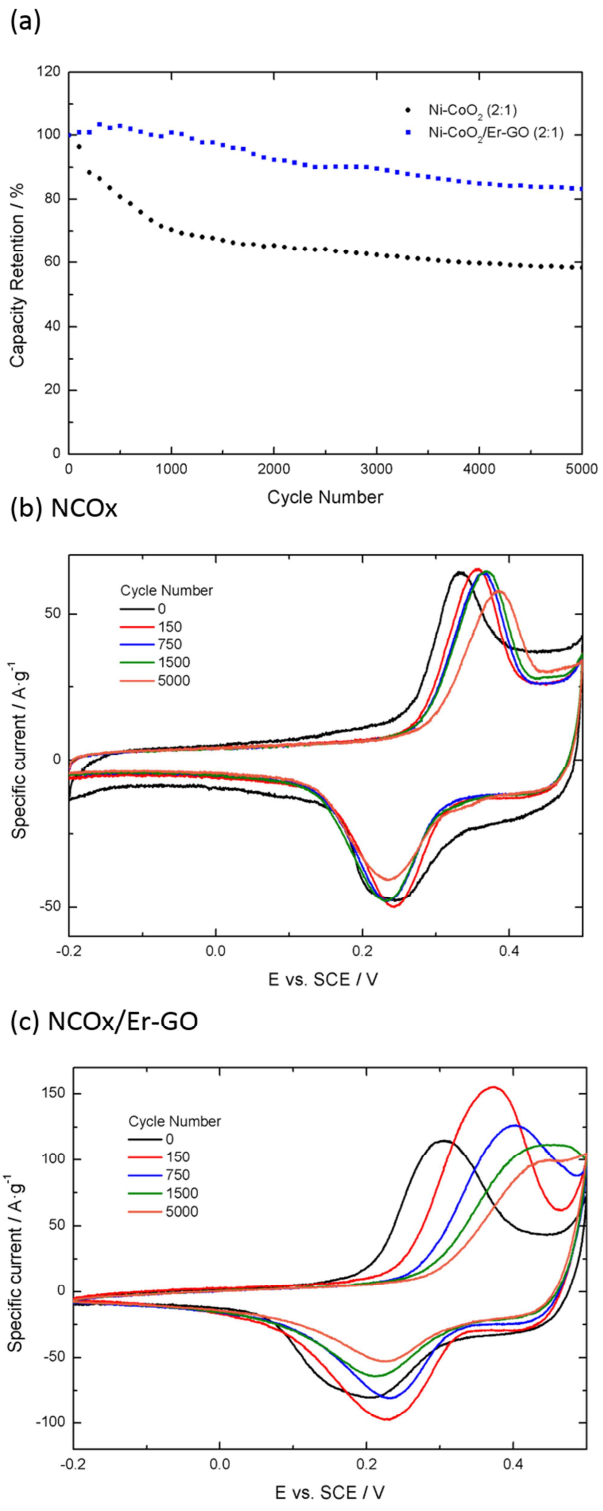

Fig. 5. (**a**) Capacity Retention comparison obtained during cycling at 8 $A \cdot g^{-1}$ during 5000 cycles measured in KOH 1M and Cyclic Voltammetry response degradation at 50 $mV \cdot s^{-1}$ with cycling for (**b**) NCOx and (**c**) NCOx/Er-GO measured in KOH 1M.

Results for SEM before and after cycling are depicted in Fig. 6. It is clearly visible that NCOx/Er-GO remains unchanged, while NCOx suffers from structural cracking. During the charging reaction of NCOx, there is a phase transition. This is generally associated to volume changes due to the nature of the reaction [82], increasing electrode swelling and therefore mechanical degradation. The mechanical stress, given volume variation during charge and discharge, cannot be accommodated and results in cracking. When Er-GO is introduced, nickel-cobalt oxide is homogeneously distributed on top of the carbon surface in homogeneously-distributed and smaller particles, as observed by SEM and TEM. Volume variations therefore affect smaller particles, as compared to the aggregates in NCOx. Consequently, the volume variation that nickel-cobalt oxide on top of reduced graphene oxide induces during charge-discharge is accommodated by the carbon matrix and as consequence cracking is inhibited.

The change in the composition is also reflected in the electrochemical response by means of cyclic voltammetry and impedance spectroscopy after 0, 150, 750, 1500 and 5000 cycles, which are depicted in Fig. 5.b,c, Fig. 7 and Fig. 8, respectively. A displacement of the peak towards more anodic values is observed during cycling.

When the atomic ratios obtained by EDS are considered, initially a Ni:Co ratio of 0.63:0.37 is obtained for both. However, after cycling, the chemical composition evolves to a ratio of 0.60:0.40 in the case of NCOx, while resulting in a value of 0.64:0.36 for NCOx /Er-GO. This would indicate a loss of nickel during the durability test for the former composite, while the composition for the Er-GO based composite is kept. From EDS it can be concluded that chemical dissolution and variation of the composition of the electrode material occurs, but this behaviour is not completely understood. Normally, the instability of Ni-Co LDH materials arises from dissolution of cobalt ions, resulting in composites with greater nickel concentration [51,83–85]. Consequently, the peaks tend to vary to more anodic values, where the potential of NiO is located. This is also observed in the present cyclic voltammetry but is contradictory

with the present EDS results. Thus, as a result of the semi-quantitative nature of EDS and the anomaly in the results, further analysis in this regard shall be done.

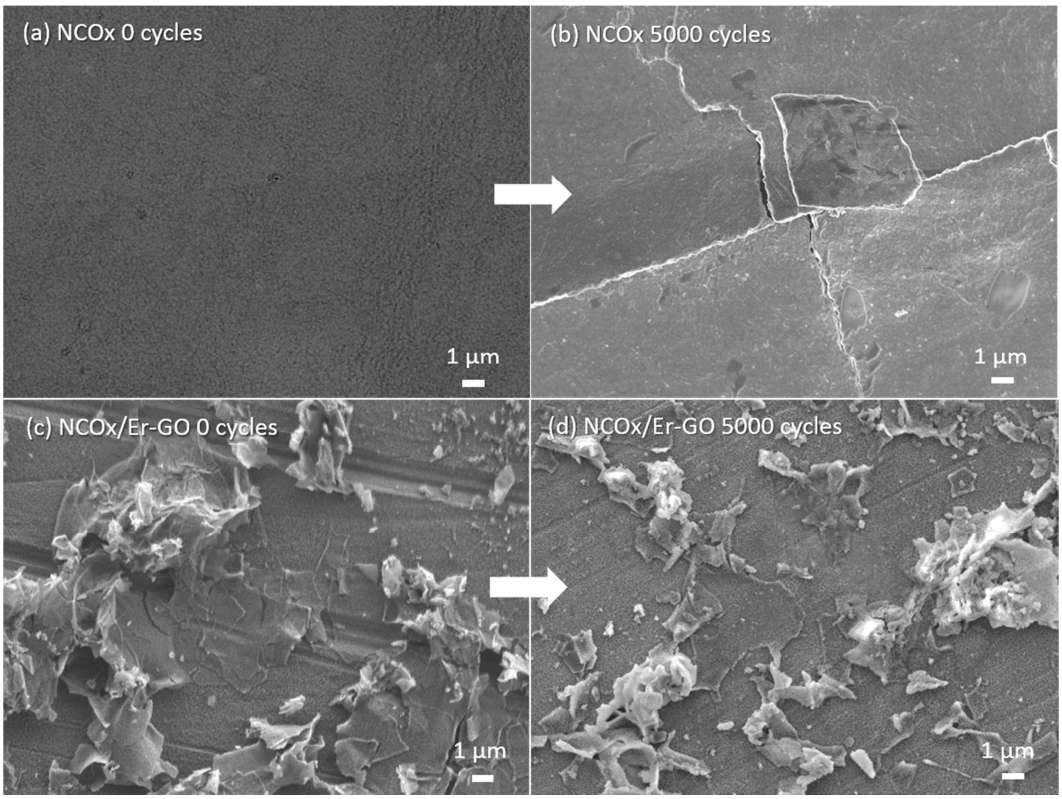

Fig. 6. Scanning electron microscopy images showing the degradation effects in the initial composites (**a**) NCOx and (**c**) NCOx/Er-GO after 5000 cycles of charge-discharge at a current density of 8 A/g for (**b**) NCOx and (**d**) NCOx/Er-GO.

For energy storage materials with faradaic response, it is important to evaluate their EIS response at least in two different potentials, charged and discharged conditions, since different and relevant information can be obtained from both. For that reason, the EIS spectra were obtained at -0.2 V and 0.45 V (vs. SCE). The direct comparison of the EIS response during the first cycle is depicted in Fig. S5, although the evolution of the EIS spectra after 0, 150, 750, 1500 and 5000 cycles of galvanostatic charge-discharge cycling at $8A \cdot g^{-1}$ is depicted in Fig.7 and Fig.8.

The charge mechanism involves the transformation of semi-conductive nickel-cobalt oxide into a conductive oxyhydroxide [86]. Thus, a reduction in the film charge-transfer resistance from the discharged to charged condition is expected. This is visible by the appearance of a second plateau with lower resistance at low frequencies in the modulus of resistance vs. frequency plot and the decrease in the diameter of the semi-circle in the Nyqusit plots. Moreover, in the discharged condition, a less kinetically favoured process at low frequencies is present, but it disappears when the material is charged. The material's behaviour is, as usually reported for impedance spectroscopy [41,87,88], separated in the contribution of two time-constants, namely, double layer capacitance (superficial charges and resistance associated in the charge transfer change from ionic conductor to electron conduction in a solid) and film capacitance. This is reflected in the equivalent circuit presented in Fig. 7d. With cycling, the material becomes more resistive for both charge-states of the material, which leads to increased values of the second resistive plateau in the modulus vs. frequency plot and an increasing semi-circle in Nyquist plots. Moreover, low-frequency resistive phenomena become more relevant with cycling when the electrode is discharged, at -0.2V, as observed in the phase angle plot.

A graphic analysis of the results obtained for the mathematical fitting of impedance results is presented in Fig. S6. Considering the values obtained for NCOx, three main features can be observed. First, the increase in the admittance of the constant phase element (CPE) assigned to the double-layer when the electrode is charged. Second, the drastic reduction of film resistance when the material is converted from oxide to oxyhydroxide (and an associated increase in film admittance). Third, the overall increase in resistance with cycling. The variation of film admittance and resistance for the material at -0.2 V and at 0.45 V is expected and associated to the oxidation state change for nickel and cobalt and change in conductivity when the phase is transformed from oxide to oxyhydroxide.

There are several potential explanations for the evolution/degradation of these materials with cycling. In the case of NCOx it shall be considered that: 1) There is a progressive decay of capacity, more intense during the first cycles. 2) Double layer and equivalent series resistance are maintained (with a very small increase) throughout cycling. 3) Film resistance increases with cycling. 4) There is an evident material degradation as observed by SEM. Thus, the increase in resistance may be related to the increased strain induced by the collapse of the superficial structure. 5) There is a variation in the chemical composition, which is reflected by EDS and the peak potential variation in cyclic voltammetry. 6) Oxygen evolution reaction is close to the maximum charge potential and may contribute to parasitic reactions, inducing capacity decay. Also, OER could mechanically degrade the material, if O_2 is produced. 7) Cycling displaces the anodic peak to higher potentials as observed by cyclic voltammetry. Thus, the electrochemical reaction is closer to the OER potentially being more affected by it as long as the cycling evolves. 8) Low-frequency phenomena obtained at -0.2 V intensifies under consecutive cycling.

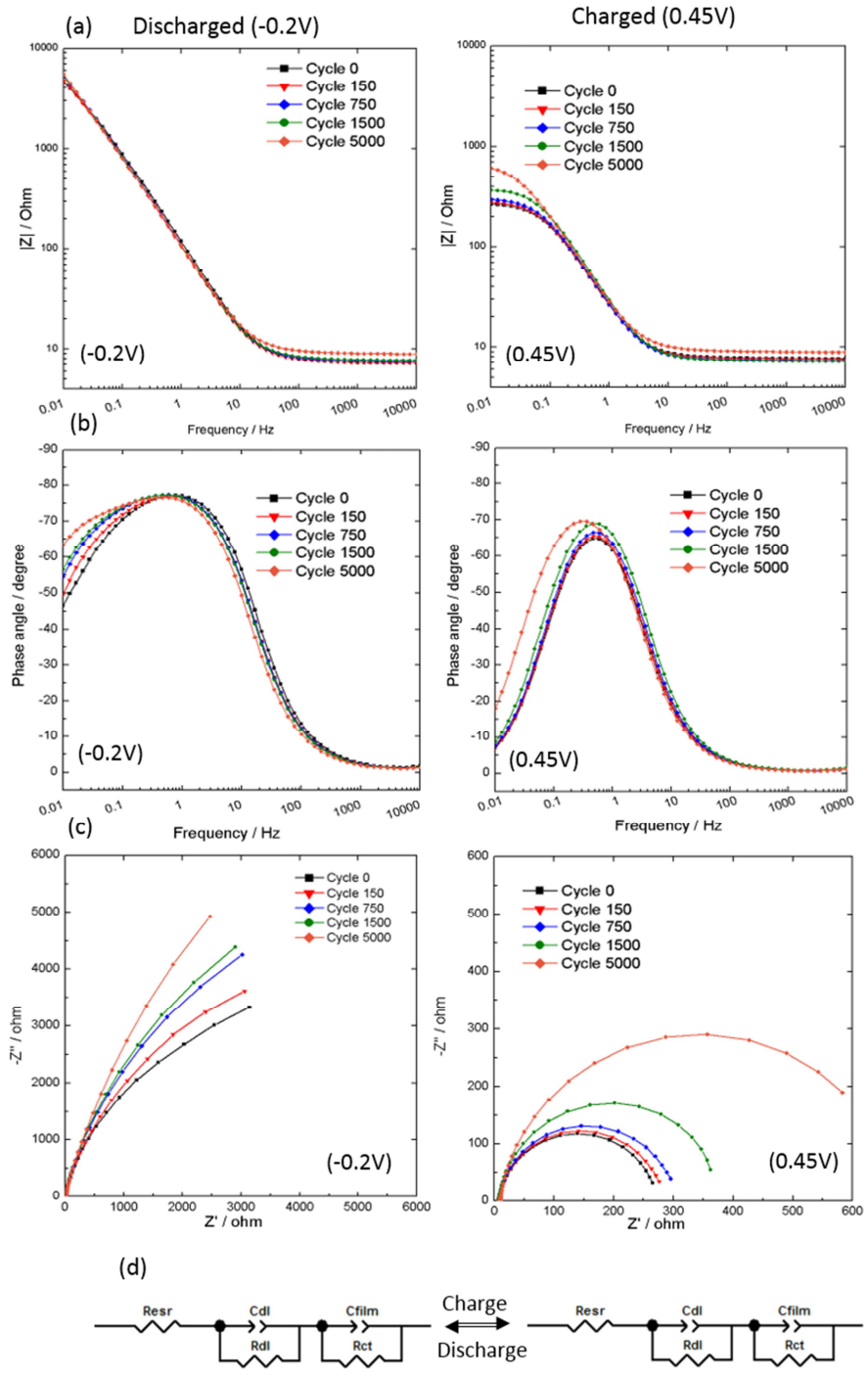

Fig. 7. (**a**) and (**b**) Bode and (**c**) Nyquist Electrochemical Impedance Spectra for NCOx composite material after 0, 150, 750, 1500 and 5000 cycles of Galvanostatic Charge Discharge at 8 A/g for both discharged (-0.2V, left) and charged (0.45V, right) potentials. (**d**) Equivalent circuit model used in the fitting of the impedance spectra acquired for NCOx at -0.2V (discharged) and 0.45V (charged).

When reduced graphene oxide is introduced (Fig. 8), a similar behaviour to that of NCOx is observed. Nonetheless, there are several features that are different and shall be considered: 1) ESR is slightly lower than for NCOx. 2) Double layer resistance has significantly lower values. The measured resistance is normalized to the apparent experimental area (1 cm^2) but the real area includes a much more extensive surface area, as a consequence of the Er-GO matrix. Thus, these calculated values are apparent resistance values that should be multiplied by the real active area of the material, which would probably lead to similar values to those obtained for NCOx. 3) Double layer resistance is maintained at both charge-states of the material. 4) Film resistance is much higher for the discharged condition while lower for the charged condition as compared to NCOx. This may be related to a greater exposure of the nickel-cobalt material to the electrolyte induced by Er-GO and the change in the conductivity in the charging process. In a similar manner, there is a greater variance of the CPE admittance assigned to the film for NCOx/Er-GO, with higher conducitivity for NCOx/Er-GO compared to NCOx when the electrode is charged, while lower when the electrode is discharged. 5) An additional time constant is developed in the discharged form (-0.2V) with cycling at mid-frequencies, more evidenced when the material is cycled 750 times (Fig. 8e). This new time constant separates the capacitive contribution of the material in two components and is not as visible when the material is fully charged. This new time constant is included in the equivalent circuit for the fitting in the discharged condition after 750 cycles. 6) There is an initial decrease in film resistance when the material is charged during the first 1000 cycles. Accordingly, there is an increase in the CPE admittance as observed in the cycling test performed at 8 $A \cdot g^{-1}$. 7) No mechanical degradation or strain is identified by SEM for NCOx/Er-GO. However, there is a bigger variation in the electrochemical response observed by cyclic voltammetry when compared to NCOx, with initial increased capacity. A variation in chemical composition of the material shall also be taken into account since it is observed by EDS.

Thus, it can be considered that Er-GO acts as a matrix that accommodates strain, reducing the mechanical degradation observed by SEM. Moreover, given its increased active surface area, Er-GO induces more exposure of nickel-cobalt oxide deposited on top of it, leading to increased number of active sites. It also serves as a conductive matrix, reducing the overall electrode resistance. During the first cycles, electrolyte penetration may reach initially inaccessible pores that later become active sites, leading to an initial increase in capacity. Besides, the observed increase in resistance with cycling is much smaller in absolute terms in the case of the Er-GO containing material. While Ni-Co oxide is affected by mechanical degradation, increasing the measured resistance, NCOx/Er-GO initially increases its capacity by electrolyte penetration during the first 1000 cycles and inhibits mechanical stress.

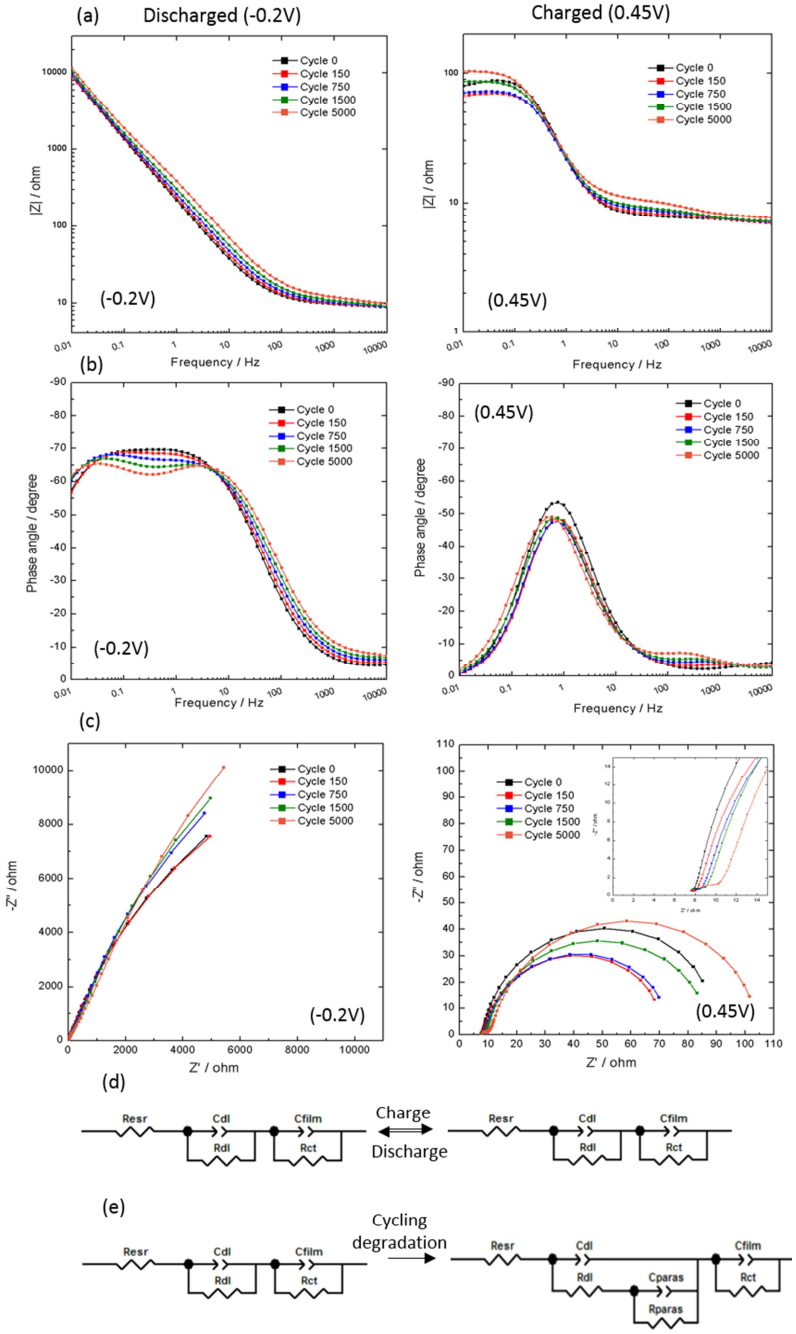

Fig. 8. (**a**) and (**b**) Bode and (**c**) Nyquist Electrochemical Impedance Spectra for NCOx/Er-GO composite material after 0, 150, 750, 1500 and 5000 cycles of Galvanostatic Charge Discharge at 8 A/g for both discharged (-0.2V, left) and charged (0.45V, right) potentials. (**d**) Equivalent circuit model used in the fitting of the impedance spectra acquired for NCOx/Er-GO at -0.2V (discharged) and 0.45V (charged) (**e**) Equivalent circuit model used in the fitting of impedance spectra acquired for NCOx/Er-GO at -0.2V with cycling after 750, 1500 and 5000 cycles.

However, the increased exposure to the electrolyte leads to the formation and stabilization of a secondary parasitic phase, as observed by the new time constant by EIS. This parasitic reaction, considering previous reports, is likely to be the formation of a nickel-cobalt hydroxide phase. When material is charged, an oxyhydroxide phase is formed and, when this reaction is reversed, it may generate a hydroxide phase considering that the reaction takes place in alkali media and taking into account that nickel-cobalt hydroxide is also transformed into an oxyhydroxide phase during charging, as exemplified in equations 3 and 4 [89]:

$$\alpha\text{-}Ni_xCo_{1-x}(OH)_2(2NO_3^-, CO_3^{2-})_{(1-x)/2}(H_2O)_{0.5} + (0.5-y)(Na^+, K^+) \longleftrightarrow \gamma\text{-}Ni_xCo_{1-x}OO(H^+)_y(Na^+, K^+)_{(0.5-y)}(H_2O)_{0.5} + (2-y)H^+ + (1-x)/2\,(2NO_3^-, CO_3^{2-}) + (0.5+x)e^- \quad \text{(eq. 3)}$$

$$\beta\text{-}Ni_xCo_{1-x}O_2H_{1+x} \longleftrightarrow \beta\text{-}Ni_xCo_{1-x}OOH + xH^+ + xe^- \quad \text{(eq. 4)}$$

When Er-GO is introduced, the reaction presented in equation 4 is prone to occur, leading to the formation of $Ni_{1-x}Co_xO_y$ together with $Ni_xCo_{1-x}(OH)_2$. This would explain the shift in the peaks of cyclic voltammetry. Moreover, when charged, the material transforms into the oxyhydroxide form in any case and, for that reason, mid-frequency EIS response is less affected in the charged state. When discharged, given the fact that the conductivity of the oxide is higher than of the hydroxide [90–92], this phenomenon increases mid-frequency resistance.

Finally, a similar decay in the capacity of NCOx to NCOx/Er-GO (once the material is stabilized) occurs, associated to similar degradation processes. In fact, the low-frequency evolution in the discharged potential for NCOx and the variation observed by cyclic voltammetry suggests that this second phase may be also formed for NCOx, although due to the reduced electrolyte accessibility of the material and lower active surface area, it is not as relevant. Summarizing, mechanical degradation, formation of a secondary phase and OER parasitic reaction are pin-pointed as the main sources of NCOx degradation. Regarding Er-GO, there is an initial activation, produced by electrolyte penetration when Er-GO is present, that leads to an initial increase of material's capacity. When Er-GO is introduced, mechanical degradation seems to

be completely inhibited, while the formation of a secondary phase is promoted. As a result, the capacity decay, reduced to a 16.8% after 5000 cycles, is caused by this instability of the oxide phase alongside the effect of the OER parasitic reaction. These results are summarized in Fig. S7.

4. Conclusions

Cobalt-nickel oxide in combination with electrochemically reduced graphene oxide was successfully prepared by electrodeposition followed by thermal treatment. The inclusion of reduced graphene oxide to the mixed oxide greatly improved energy storage capability, that increased from 113 $mA{\cdot}h{\cdot}g^{-1}$ to 180 $mA{\cdot}h{\cdot}g^{-1}$. Cycling stability after 5000 cycles, and subsequent capacity retention, increased from 58% to 83%. The faradaic efficiency was improved from 0.88 to 1.01 and the rate capability of the composite rose from 78% to 84%. Finally, a detailed study on the degradation mechanism by means of electrochemical impedance spectroscopy has been performed in combination with cyclic voltammetry, scanning electron microscopy and electron diffraction spectroscopy. EIS evidenced conductivity changes during the oxidation process of the material and the appearance of a second time constant for NCOx/Er-GO at -0.2V after cycling that might be associated to a new phase composed of nickel-cobalt hydroxide. Thus, there are three main key observations related to the cycling stability of the material: 1) Variation in peak potential by cyclic voltammetry. 2) Mechanical degradation observed by SEM. 3) New time mid-frequency constant in EIS spectra. These results suggest that degradation mechanisms, and consequent capacity fade, can be attributed to cracking caused by strain during charge and discharge, phase transformations that result in a parasitic phase and side reactions such as oxygen evolution. Electrochemically reduced graphene oxide serves as a conductive matrix that accommodates strain and increases the number of active sites, leading to increased electrochemical performance. Thus, a synergistic carbon-transition metal composite material

can be produced by means of a very simple route that has enhanced electrochemical performance compared to its analogous material without electrochemically reduced graphene oxide. These results pin point the potential of using reduced graphene oxide for energy storage applications.

Acknowledgements

This work has been performed in scope of International Doctoral Program in Functional Materials (**IDS-FunMat, Erasmus Mundus**) and funded by the European Union. We would like to express our gratitude to the Fundação para a Ciência e Tecnologia (FCT) for the funding under the contracts M-ERA.NET/0002/2012 and UID/QUI/00100/2013. We would also like to acknowledge Mª Joao Carmezim, Sabine Goma for performing the GIXD experiments, Catherine Denage and Philippe Dagault for their general assistance, Stephane Le Blond de Plouy for performing SEM images at the Centre de MicroCaractérisation Raimond Castaing (UMS 3623, 3 rue caroline Aigle, 31400 Toulouse, FRANCE), Marion Gayot for performing TEM images at PLACAMAT (Plateforme Aquitaine de Caractérisation des Matériaux UMS 3626 CNRS-Université de Bordeaux, 33600 Pessac, FRANCE), Philipe Legros and François Weill (PLACAMAT) for their SEM and TEM assistance.

Appendix A. Supplementary data

The following is the supplementary data related to this article:

The Supporting Information is available online and includes: SEM image of Ni-Co oxide with and without reduced graphene oxide in comparison to their hydroxide parent materials, HRTEM images of Ni-Co oxide on top of a graphene flake and its FFT; EDS mapping results for both Ni-Co oxide and Ni-Co oxide with electrochemically reduced graphene oxide; table with results of fitted XPS spectra; comparative Raman of non-reduced graphene oxide, electrochemical reduced graphene oxide, pure GO thin-film thermally treated and thermally treated electrochemically reduced graphene oxide signal in the composite material,

comparative electrochemical impedance response before cycling for nickel-cobalt oxide with and without electrochemically reduced graphene oxide and, finally, graphic analysis of fitting results for EIS.

References

[1] P. Simon, Y. Gogotsi, B. Dunn, Where Do Batteries End and Supercapacitors Begin?, Science (80-.). 343 (2014) 1210–1211. doi:10.1126/science.1249625.

[2] B.E. Conway, Transition from “supercapacitor” to “battery” behavior in electrochemical energy storage., J. Electrochem. Soc. 138 (1991) 1539–1548. doi:10.1149/1.2085829.

[3] J.H. Chae, X. Zhou, G.Z. Chen, From electrochemical capacitors to supercapatteries, Green. 2 (2012) 41–54. doi:10.1515/green-2011-0007.

[4] W. Wei, X. Cui, W. Chen, D.G. Ivey, Manganese oxide-based materials as electrochemical supercapacitor electrodes, Chem. Soc. Rev. 40 (2011) 1697–1721. doi:10.1039/C0CS00127A.

[5] M. Pumera, Graphene-based nanomaterials for energy storage, (2011) 668–674. doi:10.1039/c0ee00295j.

[6] G. Wang, Z. Lei, Z. Jiujun, A review of electrode materials for electrochemical supercapacitors, ChemsucChem. 5 (2012) 797. doi:10.1039/c1cs15060j.

[7] Y. Xie, X.W. Lou, C. Yuan, H. Bin Wu, Y. Xie, X. Wen, D. Lou, Mixed Transition-Metal Oxides : Design , Synthesis , and Energy-Related Applications, Angew. Chem. Int. Ed. Engl. 53 (2014) 1488–1504. doi:10.1002/anie.201303971.

[8] R. Della Noce, a-Co (OH) 2 / carbon nanofoam composite as electrochemical capacitor electrode operating at 2 V in aqueous medium, (2015). doi:10.1016/j.jpowsour.2015.04.131.

[9] T. Nguyen, M. Boudard, M. João Carmezim, M. Fátima Montemor, NixCo1-x(OH)2 nanosheets on carbon nanofoam paper as high areal capacity electrodes for hybrid supercapacitors, Energy. 126 (2017) 208–216. doi:10.1016/j.energy.2017.03.024.

[10] T. Nguyen, M. Boudard, M.J. Carmezim, M.F. Montemor, Layered Ni(OH)2-Co(OH)2 films prepared by electrodeposition as charge storage electrodes for hybrid supercapacitors, Sci. Rep. (2017) 1–10. doi:10.1038/srep39980.

[11] V.A. Online, T. Nguyen, M. Boudard, L. Rapenne, Morphological changes and electrochemical response of mixed nickel manganese oxides as charge storage electrodes, (2015) 10875–10882. doi:10.1039/C5TA01453K.

[12] T. Nguyen, M. Boudard, L. Rapenne, O. Chaix-pluchery, Structural evolution, magnetic properties and electrochemical response of MnCo2O4 nanosheeet films, (2015) 27844–27852. doi:10.1039/C5RA03047A.

[13] Y. Nuli, Q. Qin, Nanocrystalline transition metal ferrite thin films prepared by an electrochemical route for Li-ion batteries, J. Power Sources. 142 (2005) 292–297. doi:10.1016/j.jpowsour.2004.10.015.

[14] K. Karthikeyan, D. Kalpana, N.G. Renganathan, Synthesis and characterization of ZnCo2O4 nanomaterial for symmetric supercapacitor applications, Ionics (Kiel). 15 (2009) 107–110. doi:10.1007/s11581-008-0227-y.

[15] A. Rong, X.P. Gao, G.R. Li, T.Y. Yan, H.Y. Zhu, J.Q. Qu, D.Y. Song, Hydrothermal Synthesis of Zn2SnO4 as Anode Materials for Li-Ion Battery, J. Phys. Chem. B. 110 (2006) 14754–14760. doi:10.1021/jp062875r.

[16] G. He, L. Wang, H. Chen, X. Sun, X. Wang, Preparation and performance of NiCo2O4 nanowires-loaded graphene as supercapacitor material, Mater. Lett. 98 (2013) 164–167. doi:10.1016/j.matlet.2013.02.035.

[17] Z. Gao, W. Yang, J. Wang, N. Song, X. Li, Flexible all-solid-state hierarchical NiCo2O4/porous graphene paper asymmetric supercapacitors with an exceptional combination of electrochemical properties, Nano Energy. 13 (2015) 306–317. doi:10.1016/j.nanoen.2015.02.036.

[18] M. Li, Y. Wang, D. Wu, L. Wang, H. Yang, Hierarchical grass like NiCo2O4 nanoflakes on 3-dimensional microporous electrically conductive network with Superior Electrochemical Performance, Energy Procedia. 105 (2017) 4848–4853. doi:10.1016/j.egypro.2017.03.960.

[19] C. Yuan, J. Li, L. Hou, L. Yang, L. Shen, X. Zhang, Facile template-free synthesis of ultralayered mesoporous nickel cobaltite nanowires towards high-performance electrochemical capacitors, J. Mater. Chem. 22 (2012) 16084–16090. doi:10.1039/c2jm32351f.

[20] Y. Lei, J. Li, Y. Wang, L. Gu, Y. Chang, H. Yuan, D. Xiao, Rapid Microwave-Assisted Green Synthesis of 3D Hierarchical Flower-Shaped NiCo2O4 Microsphere for High-Performance Supercapacitor, ACS Appl. Mater. Interfaces. 6 (2014) 1773–1780.

[21] T.Y. Wei, C.H. Chen, H.C. Chien, S.Y. Lu, C.C. Hu, A cost-effective supercapacitor material of ultrahigh specific capacitances: spinel nickel cobaltite aerogels from an epoxide-driven sol-gel process, Adv. Mater. 22 (2010) 347–351. doi:10.1002/adma.200902175.

[22] R. Della Noce, S. Eugénio, T.M. Silva, M.J. Carmezim, M.F. Montemor, α-Co(OH)2/carbon nanofoam composite as electrochemical capacitor electrode operating at 2 v in aqueous medium, J. Power Sources. 288 (2015) 234–242. doi:10.1016/j.jpowsour.2015.04.131.

[23] L. Qian, L. Gu, L. Yang, H. Yuan, D. Xiao, Direct growth of NiCo2O4 nanostructures on conductive substrates with enhanced electrocatalytic activity and stability for methanol

oxidation, Nanoscale. 3 (2013) 7388–7396. doi:10.1039/c3nr01104f.

[24] C. Yuan, J. Li, L. Hou, X. Zhang, L. Shen, X.W. Lou, Ultrathin mesoporous NiCo 2O 4 nanosheets supported on Ni foam as advanced electrodes for supercapacitors, Adv. Funct. Mater. 22 (2012) 4592–4597. doi:10.1002/adfm.201200994.

[25] Y.-M. Wang, X. Zhang, C.-Y. Guo, Y.-Q. Zhao, C.-L. Xu, H.-L. Li, Controllable synthesis of 3D NiχCo1-χ oxides with different morphologies for high-capacity supercapacitors., J. Mater. Chem. A Mater. Energy Sustain. 1 (2013) 13290–13300. doi:10.1039/c3ta12713c.

[26] J. Du, G. Zhou, H. Zhang, C. Cheng, J. Ma, W. Wei, L. Chen, T. Wang, Ultrathin Porous NiCo2O4 Nanosheet Arrays on Flexible Carbon Fabric for High-Performance Supercapacitors, (2013) 7405–7409.

[27] X. Wang, W.S. Liu, X. Lu, P.S. Lee, Dodecyl sulfate-induced fast faradic process in nickel cobalt oxide–reduced graphite oxide composite material and its application for asymmetric supercapacitor device, J. Mater. Chem. 22 (2012) 23114. doi:10.1039/c2jm35307e.

[28] Z. Fan, J. Chen, K. Cui, F. Sun, Y. Xu, Y. Kuang, Preparation and capacitive properties of cobalt – nickel oxides / carbon nanotube composites, Electrochim. Acta. 52 (2007) 2959–2965. doi:10.1016/j.electacta.2006.09.029.

[29] Q. Li, J. Cheng, B. Wang, L. Zhang, Activated carbon modified by CNTs/Ni-Co oxide as hybrid electrode materials for high performance supercapacitors., IEEE Trans. Nanotechnol. 13 (2014) 557–562. doi:10.1109/TNANO.2014.2310512.

[30] M. Wu, S. Meng, Q. Wang, W. Si, W. Huang, X. Dong, Nickel-Cobalt Oxide Decorated 3D Graphene as an Enzyme Mimic for Glucose and Calcium Detection Nickel-Cobalt Oxide Decorated 3D Graphene as an Enzyme Mimic for Glucose and Calcium Detection, Appl.

Mater. Interfaces. (2015). doi:10.1021/acsami.5b06299.

[31] E. Umeshbabu, G. Rajeshkhanna, G.R. Rao, Effect of solvents on the morphology of NiCo 2 O 4 / graphene nanostructures for electrochemical pseudocapacitor application, J. Solid State Electrochem. (2016) 1837–1844. doi:10.1007/s10008-015-3022-5.

[32] H.-W. Wang, Z.-A. Hu, Y.-Q. Chang, Y.-L. Chen, H.-Y. Wu, Z.-Y. Zhang, Y.-Y. Yang, Design and synthesis of NiCo2O4–reduced graphene oxide composites for high performance supercapacitors, J. Mater. Chem. 21 (2011) 10504. doi:10.1039/c1jm10758e.

[33] M. Yu, J. Chen, J. Liu, S. Li, Y. Ma, J. Zhang, J. An, Mesoporous NiCo2O4 nanoneedles grown on 3D graphene-nickel foam for supercapacitor and methanol electro-oxidation, Electrochim. Acta. 151 (2015) 99–108. doi:10.1016/j.electacta.2014.10.156.

[34] D. Carriazo, J. Patiño, M.C. Gutiérrez, M.L. Ferrer, F. del Monte, Microwave-assisted synthesis of NiCo2O4–graphene oxide nanocomposites suitable as electrodes for supercapacitors, RSC Adv. 3 (2013) 13690. doi:10.1039/c3ra42610f.

[35] A. Adán-más, R.G. Duarte, T.M. Silva, L. Guerlou-demourgues, M. Fátima, G. Montemor, Enhancement of the Ni-Co hydroxide response as Energy Storage Material by Electrochemically Reduced Graphene Oxide, Electrochim. Acta. 240 (2017) 323–340. doi:10.1016/j.electacta.2017.04.070.

[36] C. Zhang, T. Kuila, N.H. Kim, S. Hee, J.H. Lee, Facile preparation of flower-like NiCo2O4 / three dimensional graphene foam hybrid for high performance supercapacitor electrodes, Carbon N. Y. 89 (2015) 328–339. doi:10.1016/j.carbon.2015.03.051.

[37] V.H. Nguyen, J. Shim, Three-dimensional nickel foam/graphene/NiCo2O4 as high-performance electrodes for supercapacitors, J. Power Sources. 273 (2015) 110–117. doi:10.1016/j.jpowsour.2014.09.031.

[38] J. Zhang, F. Liu, J.P. Cheng, X.B. Zhang, Binary Nickel-cobalt Oxides Electrode Materials

for High-performance Supercapacitors : Influence of its Composition and Porous Nature, ACS Appl. Mater. Interfaces. 7 (2015) 17630–17640.

[39] V. Srinivasan, J.W. Weidner, Studies on the capacitance of nickel oxide films: effect of heating temperature and electrolyte concentration, J. Electrochem. Soc. 147 (2000) 880–885. doi:10.1149/1.1393286.

[40] D.P. Lapham, a C.C. Tseung, The effect of firing temperature, preparation technique and composition on the electrical properties of the nickel cobalt oxide series NixCo1-xOy, J. Mater. Sci. 39 (2004) 251–264. doi:10.1023/B:JMSC.0000007751.14703.4b.

[41] A.N. Naveen, S. Selladurai, Novel low temperature synthesis and electrochemical characterization of mesoporous nickel cobaltite-reduced graphene oxide (RGO) composite for supercapacitor application., Electrochim. Acta. 173 (2015) 290–301. doi:10.1016/j.electacta.2015.05.072.

[42] G. Ma, M. Yang, C. Li, H. Tan, L. Deng, S. Xie, F. Xu, L. Wang, Y. Song, Preparation of spinel nickel-cobalt oxide nanowrinkles/reduced graphene oxide hybrid for nonenzymatic glucose detection at physiological level, Electrochim. Acta. 220 (2016) 545–553. doi:10.1016/j.electacta.2016.10.163.

[43] K.S. Novoselov, V.I. Fal'ko, L. Colombo, P.R. Gellert, M.G. Schwab, K. Kim, A roadmap for graphene., Nature. 490 (2012) 192–200. doi:10.1038/nature11458.

[44] A. Adán-Más, D. Wei, Photoelectrochemical Properties of Graphene and Its Derivatives, Nanomaterials. 3 (2013) 325–356. doi:10.3390/nano3030325.

[45] I. Jung, D.A. Dikin, R.D. Piner, R.S. Ruoff, Tunable Electrical Conductivity of Individual Graphene Oxide Sheets Reduced At "Low" Temperatures, Nano Lett. 8 (2008) 4283.

[46] T. Schwamb, B.R. Burg, N.C. Schirmer, D. Poulikakos, An electrical method for the measurement of the thermal and electrical conductivity of reduced graphene oxide

nanostructures, Nanotechnology. 20 (2009). doi:10.1088/0957-4484/20/40/405704.

[47] L. Ma, X. Shen, Z. Ji, X. Cai, G. Zhu, K. Chen, Porous NiCo2O4 nanosheets/reduced graphene oxide composite: Facile synthesis and excellent capacitive performance for supercapacitors, J. Colloid Interface Sci. 440 (2015) 211–218. doi:10.1016/j.jcis.2014.11.008.

[48] G. Greczynski, L. Hultman, C 1s Peak of Adventitious Carbon Aligns to the Vacuum Level: Dire Consequences for Material's Bonding Assignment by Photoelectron Spectroscopy, ChemPhysChem. 18 (2017) 1507–1512. doi:10.1002/cphc.201700126.

[49] D.J. Miller, M.C. Biesinger, N.S. McIntyre, Interactions of CO2 and CO at fractional atmosphere pressures with iron and iron oxide surfaces: One possible mechanism for surface contamination?, Surf. Interface Anal. 33 (2002) 299–305. doi:10.1002/sia.1188.

[50] C. Faure, C. Delmas, P. Willmann, Preparation and characterization of cobalt-substituted α-nickel hydroxide stable in KOH medium Part II. α-Hydroxide with a turbostratic structure, J. Power Sources. 35 (1991) 263–277. doi:http://dx.doi.org/10.1016/0378-7753(91)80111-A.

[51] C. Delmas, C. Faure, Y. Borthomieu, The effect of cobalt on the chemical and electrochemical behaviour of the nickel hydroxide electrode, Mater. Sci. Eng. B. 13 (1992) 89–96. doi:10.1016/0921-5107(92)90147-2.

[52] M.C. Biesinger, B.P. Payne, A.P. Grosvenor, L.W.M. Lau, A.R. Gerson, R.S.C. Smart, Resolving surface chemical states in XPS analysis of first row transition metals, oxides and hydroxides: Cr, Mn, Fe, Co and Ni, Appl. Surf. Sci. 257 (2011) 2717–2730. doi:10.1016/j.apsusc.2010.10.051.

[53] M.C. Biesinger, B.P. Payne, L.W.M. Lau, A. Gerson, R.S.C. Smart, X-ray photoelectron spectroscopic chemical state Quantification of mixed nickel metal, oxide and hydroxide

systems, Surf. Interface Anal. 41 (2009) 324–332. doi:10.1002/sia.3026.

[54] A.P. Grosvenor, M.C. Biesinger, R.S.C. Smart, N.S. McIntyre, New interpretations of XPS spectra of nickel metal and oxides, Surf. Sci. 600 (2006) 1771–1779. doi:10.1016/j.susc.2006.01.041.

[55] H.A.E. Hagelin-Weaver, J.F. Weaver, G.B. Hoflund, G.N. Salaita, Electron energy loss spectroscopic investigation of Ni metal and NiO before and after surface reduction by Ar+bombardment, J. Electron Spectros. Relat. Phenomena. 134 (2004) 139–171. doi:10.1016/j.elspec.2003.10.002.

[56] A.G. Marrani, V. Novelli, S. Sheehan, D.P. Dowling, D. Dini, Probing the Redox States at the Surface of Electroactive Nanoporous NiO Thin Films, (2014).

[57] R.P. Sen, G.S. K., Calculation of multiplet structure of core p-vacancy levels. II, Phys. Rev. B. 12 (1975).

[58] J. Yang, H. Liu, W.N. Martens, R.L. Frost, Synthesis and Characterization of Cobalt Hydroxide , Cobalt Oxyhydroxide , and Cobalt Oxide Nanodiscs, J. Phys. Chem. C. 114 (2010) 111–119.

[59] L. Ma, X. Shen, H. Zhou, Z. Ji, K. Chen, G. Zhu, High performance supercapacitor electrode materials based on porous NiCo2O4 hexagonal nanoplates/reduced graphene oxide composites, Chem. Eng. J. 262 (2015) 980–988. doi:10.1016/j.cej.2014.10.079.

[60] W. Huang, S. Ding, Y. Chen, W. Hao, X. Lai, J. Peng, J. Tu, Y. Cao, X. Li, 3D NiO hollow sphere/reduced graphene oxide composite for high-performance glucose biosensor, Sci. Rep. 7 (2017) 5220. doi:10.1038/s41598-017-05528-1.

[61] S.P. Lim, N.M. Huang, H.N. Lim, Solvothermal synthesis of SnO2/graphene nanocomposites for supercapacitor application., Ceram. Int. 39 (2013) 6647–6655. doi:10.1016/j.ceramint.2013.01.102.

[62] H. Wang, H. Yi, X. Chen, X. Wang, Asymmetric supercapacitors based on nano-architectured nickel oxide/graphene foam and hierarchical porous nitrogen-doped carbon nanotubes with ultrahigh-rate performance, J. Mater. Chem. A. 2 (2014) 3223–3230. doi:10.1039/C3TA15046A.

[63] J. Hong, M.K. Park, E.J. Lee, D. Lee, D.S. Hwang, S. Ryu, Origin of New Broad Raman D and G Peaks in Annealed Graphene, Sci. Rep. 3 (2013) 1–5. doi:10.1038/srep02700.

[64] R. Kumar, B.R. Mehta, M. Bhatnagar, R. S, S. Mahapatra, S. Salkalachen, P. Jhawar, Graphene as a transparent conducting and surface field layer in planar Si solar cells, Nanoscale Res. Lett. 9 (2014) 349. doi:10.1186/1556-276X-9-349.

[65] J.-H. Zhong, A.-L. Wang, G.-R. Li, J.-W. Wang, Y.-N. Ou, Y.-X. Tong, Co3O4/Ni(OH)2 composite mesoporous nanosheet networks as a promising electrode for supercapacitor applications, J. Mater. Chem. 22 (2012) 5656. doi:10.1039/c2jm15863a.

[66] Z. Liu, K. Xiao, Q. Xu, N. Li, Y. Su, H. Wang, S. Chen, Fabrication of hierarchical flower-like super-structures consisting of porous NiCo2O4 nanosheets and their electrochemical and magnetic properties, RSC Adv. 3 (2013) 4372. doi:10.1039/c3ra23084h.

[67] Y. Chuminjak, S. Daothong, A. Kuntarug, High-performance Electrochemical Energy Storage Electrodes Based on Nickel Oxide-coated Nickel Foam Prepared by Sparking Method, Electrochim. Acta. 238 (2017) 298–309. doi:10.1016/j.electacta.2017.03.190.

[68] H. Zhang, X. Zhang, D. Zhang, X. Sun, H. Lin, C. Wang, One-Step Electrophoretic Deposition of Reduced Graphene Oxide and Ni(OH)2 Composite Films for Controlled Syntheses Supercapacitor Electrodes, J. Phys. Chem. B. 117 (2013) 1616–1627.

[69] Y. Bai, M. Liu, J. Sun, L. Gao, Fabrication of Ni-Co binary oxide/reduced graphene oxide composite with high capacitance and cyclicity as efficient electrode for supercapacitors,

Ionics (Kiel). 22 (2016) 535–544. doi:10.1007/s11581-015-1576-y.

[70] X. Lu, X. Huang, S. Xie, T. Zhai, C. Wang, P. Zhang, M. Yu, W. Li, C. Liang, Y. Tong, Controllable synthesis of porous nickel–cobalt oxide nanosheets for supercapacitors, J. Mater. Chem. 22 (2012) 13357. doi:10.1039/c2jm30927k.

[71] R.P. Silva, S. Eugénio, R. Duarte, T.M. Silva, M.J. Carmezim, M.F. Montemor, Co-Electrochemical Response of 70Co-30Ni Highly Branched 3D-Dendritic Structures for Charge Storage Electrodes, Electrochim. Acta. 167 (2015) 13–19. doi:10.1016/j.electacta.2015.03.083.

[72] G. Wang, L. Zhang, J. Zhang, A review of electrode materials for electrochemical supercapacitors, Chem. Soc. Rev. 41 (2012) 797–828. doi:Doi 10.1039/C1cs15060j.

[73] T. Brousse, D. Belanger, J.W. Long, To Be or Not To Be Pseudocapacitive?, J. Electrochem. Soc. 162 (2015) A5185–A5189. doi:10.1149/2.0201505jes.

[74] X. Wang, C. Yan, A. Sumboja, P. See, High performance porous nickel cobalt oxide nanowires for asymmetric supercapacitor, Nano Energy. 3 (2014) 119–126. doi:10.1016/j.nanoen.2013.11.001.

[75] X. Zhao, X. Li, Y. Huang, Z. Su, J. Long, S. Zhang, J. Sha, T. Wu, R. Wang, Electrochemical performances of graphene nanoribbons interlacing hollow NiCo oxide nanocages, J. Nanoparticle Res. 19 (2017). doi:10.1007/s11051-017-4078-1.

[76] X. Wang, W.S. Liu, X. Lu, P.S. Lee, Dodecyl sulfate-induced fast faradic process in nickel cobalt oxide–reduced graphite oxide composite material and its application for asymmetric supercapacitor device, J. Mater. 22 (2012) 23114–23119. doi:10.1039/c2jm35307e.

[77] V.H. Nguyen, C. Lamiel, J.J. Shim, Mesoporous 3D graphene@NiCo2O4 arrays on nickel foam as electrodes for high-performance supercapacitors, Mater. Lett. 170 (2016) 105–

109. doi:10.1016/j.matlet.2016.02.017.

[78] M. Yu, J. Chen, J. Liu, S. Li, Y. Ma, J. Zhang, J. An, Mesoporous NiCo2O4nanoneedles grown on 3D graphene-nickel foam for supercapacitor and methanol electro-oxidation, Electrochim. Acta. 151 (2015) 99–108. doi:10.1016/j.electacta.2014.10.156.

[79] M. Rajkumar, C.T. Hsu, T.H. Wu, M.G. Chen, C.C. Hu, Advanced materials for aqueous supercapacitors in the asymmetric design, Prog. Nat. Sci. Mater. Int. 25 (2015) 527–544. doi:10.1016/j.pnsc.2015.11.012.

[80] D.B. Murray, J.G. Hayes, Cycle testing of supercapacitors for long-life robust applications, IEEE Trans. Power Electron. 30 (2015) 2505–2516. doi:10.1109/TPEL.2014.2373368.

[81] S. Saxena, C. Le Floch, J. Macdonald, S. Moura, Quantifying EV battery end-of-life through analysis of travel needs with vehicle powertrain models, J. Power Sources. 282 (2015) 265–276. doi:10.1016/j.jpowsour.2015.01.072.

[82] P.J. Tsai, S.L.I. Chan, Nickel-based batteries: materials and chemistry, Woodhead Publishing Limited, 2013. doi:10.1533/9780857097378.3.309.

[83] V. Pralong, A. Delahaye-Vidal, Y. Chabre, B. Beaudoin, J.-M. Tarascon, The Outcome of Cobalt in the Nickel–Cobalt Oxyhydroxide Electrodes of Alkaline Batteries, J. Solid State Chem. 162 (2001) 270–281. doi:10.1006/jssc.2001.9293.

[84] C. Faure, Y. Borthomieu, C. Delmas, M. Fouassier, Infrared characterization of turbostratic α- and well crystallized α*-cobalted nickel hydroxides, J. Power Sources. 36 (1991) 113–125. doi:http://dx.doi.org/10.1016/0378-7753(91)80008-L.

[85] C. Faure, C. Delmas, P. Willmann, Electrochemical behavior of α-cobalted nickel hydroxide electrodes, J. Power Sources. 36 (1991) 497–506. doi:http://dx.doi.org/10.1016/0378-7753(91)80075-9.

[86] S.P. Mitoff, Electrical conductivity and thermodynamic equilibrium in nickel oxide, J. Chem. Phys. 727 (1961) 882–889. doi:10.1063/1.1701231.

[87] B.K. Kim, V. Chabot, A. Yu, Carbon nanomaterials supported Ni(OH)2/NiO hybrid flower structurefor supercapacitor, Electrochim. Acta. 109 (2013) 370–380. doi:10.1016/j.electacta.2013.07.119.

[88] B. Yan, M. Li, X. Li, Z. Bai, L. Dong, D. Li, Electrochemical impedance spectroscopy illuminating performance evolution of porous core-shell structured nickel/nickel oxide anode materials, Electrochim. Acta. 164 (2015) 55–61. doi:10.1016/j.electacta.2015.02.178.

[89] C. Faure, C. Delmas, M. Fouassier, P. Willmann, Preparation and characterization of cobalt-substituted α-nickel hydroxides stable in KOH medium Part I. α'-hydroxide with an ordered packing, J. Power Sources. 35 (1991) 249–261. doi:http://dx.doi.org/10.1016/0378-7753(91)80110-J.

[90] K. V. Rao, a. Smakula, Dielectric properties of cobalt oxide, nickel oxide, and their mixed crystals, J. Appl. Phys. 36 (1965) 2031–2038. doi:10.1063/1.1714397.

[91] P. Hermet, L. Gourrier, J. Bantignies, D. Ravot, T. Michel, S. Deabate, P. Boulet, F. Henn, Dielectric , magnetic , and phonon properties of nickel hydroxide, Phys. Rev. B. 235211 (2011) 1–10. doi:10.1103/PhysRevB.84.235211.

[92] I. Petousis, D. Mrdjenovich, E. Ballouz, M. Liu, D. Winston, W. Chen, T. Graf, T.D. Schladt, K.A. Persson, F.B. Prinz, High-throughput screening of inorganic compounds for the discovery of novel dielectric and optical materials, Sci. Data. 4 (2017) 160134. doi:10.1038/sdata.2016.134.


Micro-structural cracking
Phase transformation
OER
$Ni_xCo_{1-x}O_y$ Oxide
$Ni_xCo_{1-x}O_y$ Oxide/Er-GO